A shock recovery experiment and its implications for Mercury's surface : The effect of high pressure on porous olivine powder as a regolith analog

Stojic, Aleksandra

2020

A shock recovery experiment and its implications for Mercury's surface: The effect of high pressure on porous olivine powder as a regolith analog

Aleksandra N. Stojic [a,*], Andreas Morlok [a], Peter Tollan [b,c], Tomas Kohout [d], Jorg Hermann¨ [c], Iris Weber [a], Juulia-Gabrielle Moreau [d], Harald Hiesinger [a], Martin Sohn [e], Karin E. Bauch [a], Maximilian P. Reitze [a], Jorn Helbert¨ [f]

[a] Institut für Planetologie, Westfalische Wilhelms Universit¨ at Münster, Wilhelm-Klemm-Str. 10, D-48149 Münster, Germany ¨ [b] Institute of Geochemistry and Petrology, ETH Zürich, Clausiusstraße 25, CH-8092 Zuerich, Switzerland [c] Institute of Geological Sciences, Universitat Bern, Baltzerstra¨ ße 1+3, CH-3012 Bern, Switzerland

[d] Department of Geosciences and Geography, University of Helsinki, Gustaf Haellstroemin katu 2, FI-0014 Helsinki, Finland [e] Physikalische Chemie, University of Applied Sciences, Constantiaplatz 4, D-26723 Emden, Germany [f] Institute for Planetary Research, DLR, Rutherfordstrasse 2, D-12489 Berlin, Germany

ABSTRACT

We conducted classic dynamic high-pressure experiments on porous San Carlos (SC) olivine powder to examine if and how different shock stages modify corresponding reflectance mid−infrared (MIR) spectra. Microscopic investigation of the thin sections produced of our shocked samples indicates local peak pressures of >60 GPa along with all lower grade shock stages. Spectral analyses of optically identified shock areas were documented and compared in terms of Christiansen Feature (CF) and the position of olivine−diagnostic Reststrahlenbands (RBs). We found that one RB (fundamental vibrations of the orthosilicate-ion) of olivine occurring at 980 cm^{-1} (corresponding to ≈ 10.2 μm) shows the least energetic shift in the investigated MIR spectra and could therefore serve as a proxy for the presence of olivine in remote sensing application. Furthermore, a peak located at ≈ 1060 cm^{-1} (≈ 9.4 μm) shows a significant intensity change probably related to the degree of shock exposure or grain orientation effects, as we observe a decline in intensity of this band from our averaged reference olivine spectra of our IRIS database (diffuse reflectance measurement) down to spectra of grains showing mosaicism and recrystallized areas. We also report the presence of a weak band in some of the olivine spectra located at ≈ 1100 cm^{-1} (9.1 μm) that has an influence on the position of the CF when spectral data of olivine are averaged.

1. Introduction

BepiColombo is a joint ESA/JAXA space mission heading to Mercury that was launched in October 2018, (Benkhoff et al., 2010). MERTIS (MErcury Radiometer and Thermal Infrared Spectrometer), is an onboard spectrometer that will deliver spectral data in the range between 7 μm and 14 μm (1429 cm^{-1}–714 cm^{-1}) once the spacecraft reaches the science working orbit in 2026 and during several earlier fly-bys (Hiesinger et al., 2010, 2020). Mercury's proximity to the Sun is an extreme challenge to Earth-based telescopic observations as well as to spacecraft and their analytical tools and hardware. This explains why only scarce information is available to date about the innermost planet of the Solar System. Mariner 10 (1974) sent the first images from Mercury's surface and detected particle flux anomalies combined with a strong magnetic field (Hapke et al., 1975; Ness et al., 1974). This was a surprising finding, given that before Mariner, Mercury was thought to be geologically extinct with no substantial magnetic field to surround it. No meteorites have been found that can be unambiguously traced back to Mercury and the only available chemical information to date is that delivered by the MESSENGER mission (Nittler et al., 2011; Weber et al., 2016). From MESSENGER, we obtained, among other information, element distribution data that confirmed an overall low FeO-abundance within the planetary crust (Weider et al., 2012).

Solar wind, (micro)-meteorite bombardment, and cosmic radiation have the potential to alter an atmosphere-free planetary surface significantly. This is a phenomenon called space weathering (SW) (Hapke, 2001) and has been studied with different analytical techniques in the past; for a descriptive explanation of the observed and hypothesized influences of SW on the corresponding (mostly near infrared range (NIR)) spectra see, e.g., Domingue et al. (2014), and Pieters and Noble (2016).

SW occurs on any Solar System body that lacks a protecting atmosphere and has the potential to alter the optical and infrared fingerprint of the corresponding surface significantly. It causes reddening, darkening, a reduction of spectral features in the VIS-NIR range (Loeffler et al., 2009 (laboratory experiment); Loeffler et al., 2016 (laboratory experiment); and Noguchi et al., 2011 (natural space weathering)), effects that were documented by laboratory experiments as well as observations by space missions and ground-based tools from the Moon and asteroids (Lantz et al., 2013 (space observation), Noble et al., 2005, Pieters et al., 2000).

Mercury's unique position within the Solar System and the fact that the planet has no atmosphere to protect its surface minerals from external destructive forces, i.e., space weathering, will likely distinguish the genuine MERTIS spectra from comparable analog material of terrestrial origin (either natural or synthesized) (e.g., Noble and Pieters, 2003).

Little is known to date how SW manifests in the relevant MERTIS mid-infrared range (Weber et al., 2019, Brunetto et al., 2020). To account for this spectra-altering multi-component process - and to be able to quantify the future Mercury surface spectra more accurately, we are currently trying to assess the extent and nature of the damage that is imparted by these external factors under laboratory conditions.

Two main types of SW studies are distinguished, a) studies of naturally SW-ed samples (e.g., lunar regolith and Hayabusa I particles (Noguchi et al., 2011) and b) studies of analog material that was artificially SW-ed in the laboratory (e.g., Moroz et al., 2007). Thus, naturally SW-ed samples always represent the result of all cumulated SW factors, whereas artificially SW-ed samples can only simulate one dominating SW component, e.g., solar wind via ion irradiation experiments (Marchi et al., 2005, Brunetto, 2009, Lantz et al., 2017).

For example, lunar soils show strong evidence of re-processing during their surface exposure time on the Moon (Pillinger, 1979; Keller and McKay, 1993; Christoffersen et al., 1996). Agglutinate formation and the production of a vapor-deposited nanophase iron metal (npFe^0) patina are a result of combined distinct SW processes on the Moon. Solar wind is a quickly acting modifying

agent and together with impact-induced damage probably the main source of SW in the Solar System.

However, analog material, SW-ed artificially under laboratory conditions helps in improving our understanding of the surface-modifying processes, effective not only in the environment of Mercury, but also more broadly throughout the Solar System.

Yet, dedicated combined NIR/MIR and TEM studies of SW-ed minerals, mineral mixtures or whole rock samples remain scarce due to the intricate and costly sample preparation procedure necessary to obtain TEM samples. Studies in the context of (space) weathering published to date, either focus on the spectroscopic investigation of the induced damage of target material (mostly NIR) or on TEM observations. For example, ion irradiation experiments were carried out to simulate the effects of solar wind on analog samples and were subsequently investigated in the NIR spectral range (e.g., Marchi et al., 2005), but TEM investigation has been omitted. Impacts into bed rock and/or porous materials, e.g., porous sandstone, were studied within the framework of the MEMIN project (Kowitz et al., 2013). However, studies involved in the MEMIN context focused on the change imparted in the target material (few TEM studies (e.g., Langenhorst and Deutsch, 2012), chemical analyses (e.g, Ebert et al., 2013)), and modelling of shock wave propagation through different rocks (Güldemeister et al., 2013) rather than on the spectral properties of the impact-altered material. Therefore, Morlok et al. (2019) used experimental run products from Haman et al. (2016) to obtain MIR information from shocked terrestrial analog material.

Experiments simulating impact effects on atmosphere-free planetary bodies are extremely difficult to perform under laboratory conditions in a terrestrial environment. In this regard Mercury is a "worst case" as ambient high vacuum conditions (~ 10^{-6} mbar) are combined with extremely high daytime temperatures (~ 450 °C) extending over a long period of time in addition to high impactor velocities. Reproducing these conditions exactly is very difficult with our current technical capabilities. Moreover, the patina of impact-sublimated regolith material, which encases other regolith grains and surface-exposed bedrock, is difficult to produce due to the experimental set-up in shock recovery experiments. This is because, in order to be able to calculate shock wave reverberations accurately, the sample material and the surrounding cylinders need to be tightly packed, which would prevent the re-sublimation of sublimated material elsewhere on the sample surface.

A compromise are laser experiments (e.g., Yamada et al., 1999). Sasaki et al. (2002) were the first to successfully combine laser irradiation experiments on olivine and pyroxene grains to produce npFe^0 with subsequent transmission electron microscopic investigations of the irradiated grains. They showed that the observed reddening and overall spectral attenuation seemed to be the result of npFe^0 patina formation. Subsequently, Loeffler et al. (2009, 2016) irradiated olivine grains and successfully produced npFe^0 and documented their results spectrally (VIS, NIR) and by transmission electron microscopy (TEM) in order to obtain nanostructural information of the irradiated material. They also showed that even almost iron - free endmembers (Fo$_{99}$) that are exposed to higher cumulated doses of energy (converting to longer exposure times in space) result in the production of a vapor deposited npFe^0- layer. The corresponding NIR spectra of the irradiated material showed darkening and reddening as is observed in spectra of naturally SW-ed asteroids and the lunar regolith. However, comparing scarce TEM data of such laboratory SW-ed minerals with naturally SW-ed minerals (Noguchi et al., 2011, Matsumoto et al., 2015, Harries et al., 2016,) showed that the observed changes at nanostructural scale are not identical. Consider for example, the combined effects observed in TEM data of a cross-section of a naturally SW-ed lunar olivine grain impacted by a micrometeorite discovered by Noble et al. (2015). The grain shows the expected layer of npFe^0 on top, an effect that can be simulated in the laboratory via laser irradiation, but underneath these top layers (several tens of nanometers) this lunar olivine also shows clear evidence of impact related damage within its crystal structure, and this effect can hardly be simulated simultaneously together with a forming npFe^0 layer under laboratory conditions. How to convert laser energy exactly into impact energy is still not unambiguously defined and therefore the extent to which these experiments can accurately simulate real impact shock scenarios is not clear.

Dedicated Raman studies investigating the effect of impact pressure in naturally shocked olivine in meteorites and experimentally shocked single crystals of olivine were performed by Farrel - Turner et al. (2005), yet showing no systematic correlation between shock features visible in the shock-induced microstructures and correlated Raman spectra. Similar studies investigating the microstructural damage of olivine in dedicated shock recovery experiments were reported by Jeanloz et al. (1977), who discovered olivine glass domains in single crystals of shocked olivine grains.

Despite these inherent limitations, the experimental simulation of SW still provides invaluable information regarding specific mechanisms of surface alteration, particularly for Solar System bodies such as Mercury from which we have no physical samples. The primary goal of this study is to provide mid-infrared data of impact-related SW effects, to identify the associated spectral characteristics and thus aid in better quantifying the future MERTIS spectra. This study focuses on the impact related aspect of space weathering and its effects on the regolith formation. Micrometeorite and meteorite impacts are simulated using shock recovery techniques. The primary goal is to identify the associated spectral characteristics and, thus, aid in improving quantifying future MERTIS spectra and other remote sensing data.

The fine-grained nature of the run-products of the olivine shock recovery experiments and the heterogeneous distribution of the shock response within the run-products required the use of micro-FTIR for the investigation.

2. Materials and methods

The selected starting mineral in this study is an iron-poor olivine, which is expected to be a rock-forming mineral on most planetary bodies. The Fe/Mg-ratio is slightly higher than that expected in minerals

Finally, such spectral 'fingerprints' are of use for laboratory studies of impact materials in general, as the data can provide valuable insights for SW and shock metamorphism studies of planetary materials.
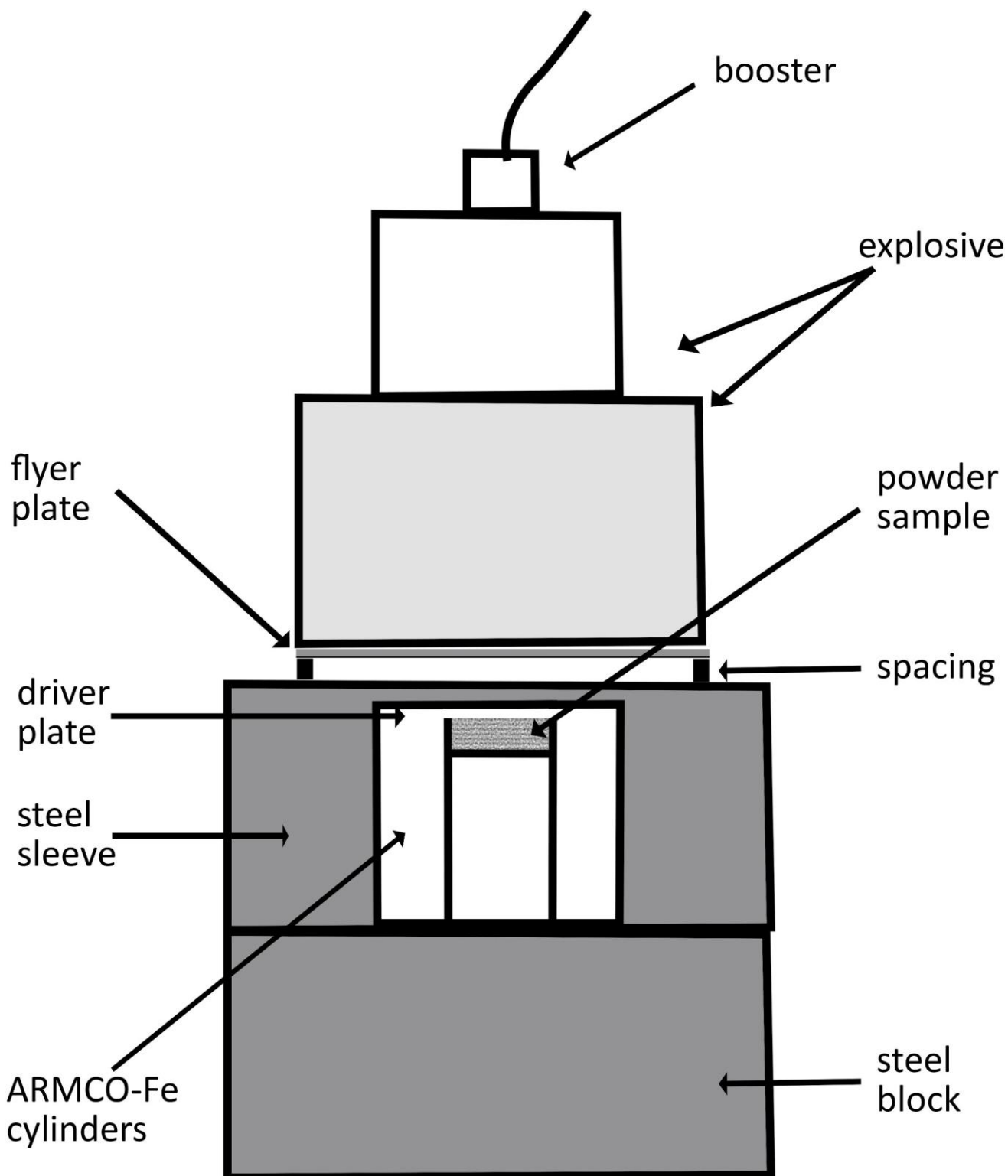
Fig. 1. Sketch of experimental set-up modified after Langenhorst & Deutsch (1994).

From bottom to top: Steel block (10 cm × 10 cm) located at the base traps the explosion momentum; Steel sleeve with white inset of ARMCO-Fe cylinders (big cylinder Ø = 5 cm; inset cylinder Ø = 2.5 cm) containing the olivine powder („sample") (grey outline in white inset). The driver plate is accelerated (white space above sample - 2 cm) toward the sample material by the flyer plate (4 mm) on top of the spacing. Explosives with booster are assembled on top.

comprising the hypothesized surface composition of Mercury (e.g., Charlier and Namur, 2019). However, the aim of this study is to investigate spectroscopic trends in experimental products that underwent simulated SW. Therefore, small differences in the starting material are acceptable. *2.1. Sample characterization*

An average chemical composition typical of San Carlos olivines (Jarosewich et al., 1980) was confirmed by quantitative SEM EDX analyses (San Carlos NIST standard). We ground three single crystals of San Carlos olivine ($\sim$ Fo$_{91}$) in an agate mortar to obtain a powder with grain sizes of up to $\sim$380 μm, which we shocked according to the description given in Section 2.2 . Clinging fines in the particulate were not removed. We used the obtained particulate material in the subsequent experimental run and refer to it as "powder" or "powder sample" hereafter.

2.2. Experimental set-up

We shocked the powdered olivine sample at the Ernst −Mach Institut (EMI) in Kandern, Germany, by accelerating a flyer plate toward the sample container using explosives. We followed the detailed description of the experimental set-up assembly given in Langenhorst & Deutsch (1994).

Two different sized ARMCO® − Fe cylinders (Ø $\sim$5 cm and $\sim$ 3 cm), one rectangular steel sleeve (10 cm × 10 cm) designed with a circular cavity (Ø = 5 cm), and a steel block (10 cm × 10 cm) were crafted in the workshop at the University of Münster. We crafted the smaller inner cylinder with a circular cavity (2.5 cm × 0.2 cm) designed to hold the olivine powder (see white ARMCO-Fe inset in Fig. 1) during the shock experiment. We filled the powder into the cavity and shielded it with a 100 μm thick Al − foil, both cylinders were put together and in turn set into a previously drilled cavity in the steel sleeve. In order to leave space between sample container assemblage and explosive, a 2 cm thick ring was placed on top, above the ARMCO-Fe cylinders. We placed a 4 mm thick flyer plate on top of the ring, which was accelerated toward the driver plate once the booster on top of the explosives was ignited. In this way forcing the driver plate into the powder, creating the shock waves that are reflected from the steel container walls producing the shock wave reverberations needed to achieve the higher pressures within the powder sample. The bottom steel block serves as a momentum trap during the detonation.

Potentially present voids between powder, Al − foil and cylinder surface prevent exact shock wave propagation calculations. Therefore, peak pressure calculations are not applicable in this case as the porous sample was not entirely in contact with the overlying Al-foil and Fe- cylinder cover. However, estimated pressures according to set-up geometry and sample material reach approximately 30 GPa in the steel container with local peak pressures of >60 GPa within the sample (Schmitt, 2000; Stoffler et al., 2018, 2019¨).
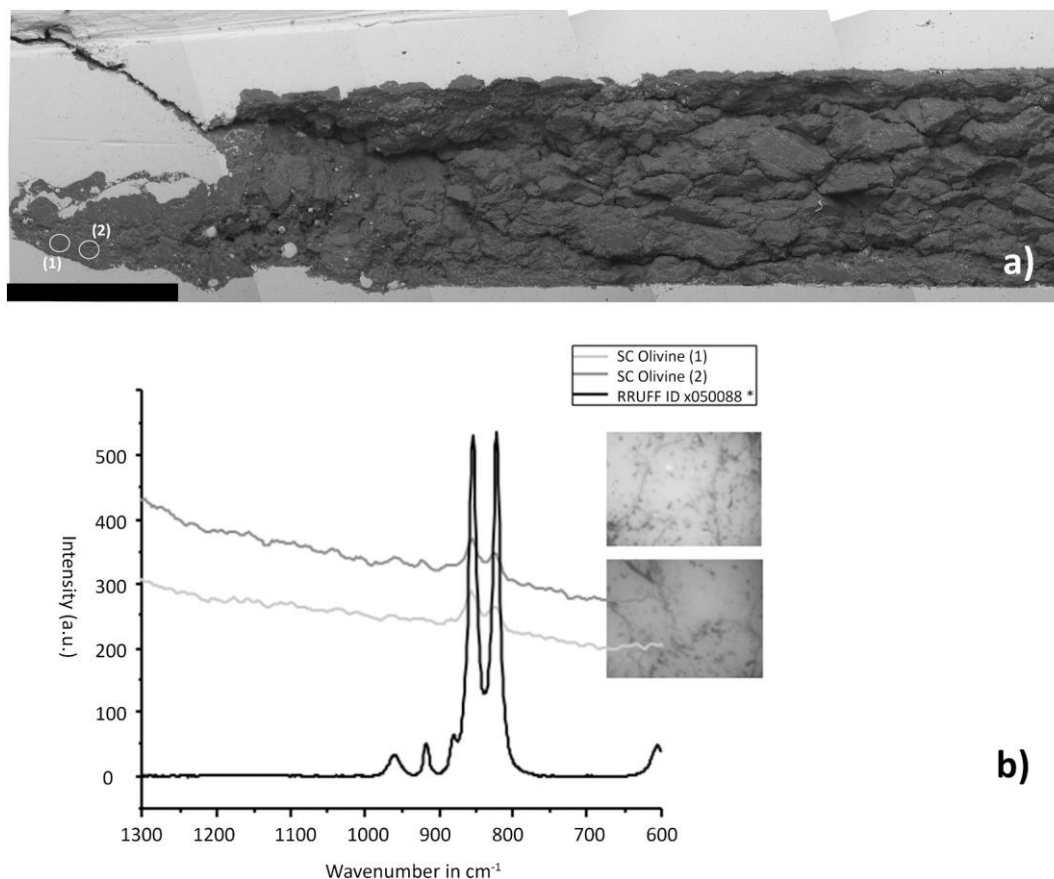

Fig. 2. a) SEM front - view of opened ARMCO Fe cylinder (bright in SEM micrograph) − the dark material within the bright confines of the cylinder is the shocked olivine powder sample. White circles (1) and (2) denote areas from which Raman spectra were obtained. Scale bar is 500 μm. Dark grey arrow (left side) signifies the propagation direction of the shock wave upon ignition during the shock experiment.

b) Raman spectra show typical forsteritic olivine double bands located at 854 cm^{-1} and 823 cm^{-1} (11.7 μm and 12.2 μm); inset reflected − light images show surfaces from which the spectra were obtained. The Raman spectra also confirm the crystallinity of the silicate matrix in which the large iron metal spots are embedded. A Raman spectrum of a SC olivine from the crystal sleuth database was implemented for comparison (black dashed spectrum) *Laetsch and Downs, 2006 [R2-11].

2.3. Post-shock characterization: polarized light and scanning electron microscope

The sample container was sawed open in our workshop and slices of the container with the shocked powder were mounted and polished carefully. We characterized a thick section of the processed material with a JEOL 6610 scanning electron microscope operated in low vacuum mode in order to avoid carbon coating (Fig. 2a). In addition, we obtained thin sections (~ 30 μm) from the sample. Mineral characteristic images of the thin section were produced using polarized light (Fig. 3a). Areas of interest for subsequent micro FTIR measurements were identified using the microscope images.

2.4. Micro FTIR

The Christiansen feature (CF) as well as Reststrahlen bands (RB) are compositional and/or mineral-specific spectral features that result from the interaction of electromagnetic waves with solid ordered matter. Variations in intensity of single RBs in normalized spectra should be indicative of processes affecting the tetrahedral (SiO^{4-}) symmetry or are "simply" grain orientation effects that are mirrored in the spectra. Planetary science is a multidisciplinary field and currently there is a different vocabulary used by groups with different scientific backgrounds. An explanation of terms like RBs and CF is given in the appendix. Also, abscissas of spectral data in this study show both units, wavenumbers (cm^{-1}) and wavelengths (μm), as both presentations are used in publications related to this field.

FTIR reflectance maps of the produced polished thin section were generated with a Bruker Hyperion 3000 equipped with a focal plane array (FPA) mapping detector combined with a 15× Cassegrain objective at the University of Bern. The native resolution projects a pixel size of ~2.7 μm onto the FPA detector (4096 spectra distributed evenly over a fixed 170 × 170 μm^2

measurement area). In order to improve spectral quality, 2 adjacent pixels were combined (binned) to produce a final resolution of ~5.4 μm. Multiple mapping grids each with cumulative scan times of roughly 1 h were distributed over the target areas of the thin section. Areas of interest were identified on the thin section and single spectra were extracted using the OPUS software. The spectral intensity of selected areas was normalized according to minimum and maximum intensity in the range between 1150 cm^{-1} and 850 cm^{-1} (8.7 μm – 11.8 μm) to better compare the rise or decline of specific RBs within a certain orientation. As all analyses were obtained from single selected grains or re-worked interstitial areas, the spectra obtained from grain fragments resemble specular reflectance measurements. We abstained from normalizing reflectance spectra in areas where intensity loss seemed to be a significant result. Non – normalized data are labelled as such where appropriate. Spectral reflectance maps of the sample surface shown in Fig. 3b were obtained by integrating over the intensity in the frequency range between 985 cm^{-1} and 978 cm^{-1} (equivalent to a range of 0.07 μm and corresponds to the spectral position of RB2).

2.5. EPMA

We measured a few selected areas of the thin section with a JEOL JXA-8530F Hyperprobe electron probe micro analyzer (EPMA) equipped with five wavelength dispersive spectrometers (WDS) to complement the spectral data with quantitative chemical analyses. The probe was operated at an acceleration voltage of 15 kV and a beam current of 15 nA. For Mg, Al, Si, Ca, Fe, Ti, Cr, and Mn in olivine and interstitial grain areas, the counting time was set to 15 s on the peak and 5 s on the background. The following natural and synthetic minerals with well-known compositions were used as standards: Jadeite (Na_2O), San Carlos Olivine (MgO), Disthene (Al_2O_3), Hypersthene (SiO_2), Sanidine (K_2O), Diopside (CaO), Fayalite (FeO), Rutile (TiO_2), Eskolaite (Cr_2O_3),
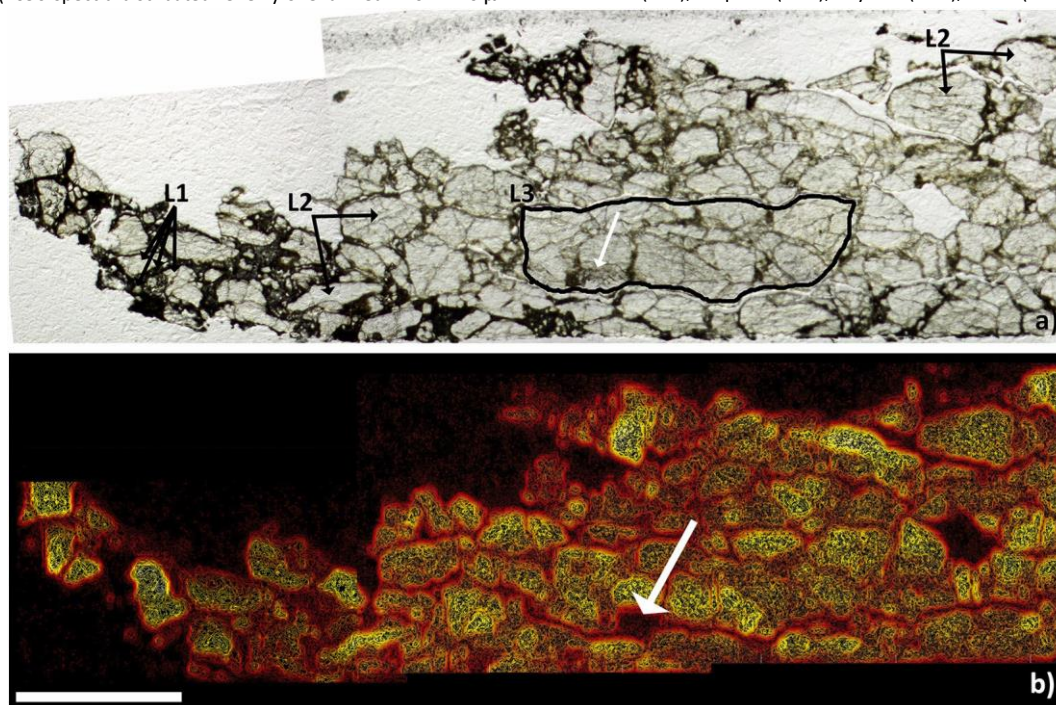

Fig. 3. a) Petrographic microscope image obtained under plane polarized light. The portion of the thin section corresponds roughly to the area depicted in Fig. 2a). L1 classified areas are mainly comprised of fractured grains (FG), interstitial material (IM) and to a lesser extent recrystallized areas (RA, see Fig. 4), L2 denotes a group of selected single grains, which show undulose extinction or mosaicism and L3 outlines an area of dense fractured grain cumulates. Scale bar is 500 μm. b) A spectral map from the thin section obtained by integrating over the intensity of RB2 (982 cm^{-1}_978 cm^{-1}/~ 10.2 μm). All shades of grey depict olivine grains. White arrow (in a) and b)) signifies the location of a pyroxene grain (contamination) that appears dark in this map. Another dark spot in the spectral map is a hole, as is clearly visible in Fig. 3a) where the corresponding location appears bright and translucent indicative of the underlying glass slide. For details and interpretation see Section 4. of the manuscript.

Table 1
EPMA spot analyses of selected sites.

a) EPMA analyses from fractured and undulose grains

	116	143	144	146	147	156	157	158	159	160	176	Ave.	s.d.
MgO	50.51	51.2	50.76	50.47	50.77	47.86	51.41	51.13	51.07	51.34	50.17	50.61	0.99
Al_2O_3	0	0	bdl	0	bdl	0	bdl	0	bdl	0	bdl		
SiO_2	40.81	40.95	40.87	40.96	40.81	40.64	40.86	40.75	40.67	40.81	40.66	40.80	0.11
CaO	0.04	bdl	bdl	0.05	0	0.07	0	0.06	0.06	bdl	0.08		
FeO	8.89	8.04	9.01	8.81	8.72	8.38	8.26	8.26	7.92	8.41	9.03	8.52	0.39
MnO	0.14	0.14	0.11	0.09	0.15	0.08	0.09	0.13	0.13	0.09	0.13		
Total	100.39	100.33	100.75	100.38	100.45	97.03	100.62	100.33	99.85	100.65	100.07		
Mg#	Fo91	Fo92	Fo91	Fo91	Fo91	Fo91	Fo92	Fo92	Fo92	Fo92			

b) EPMA analyses from the RA area

	117	118	119	120	121	122	123	124	125	126	127	128	129	135	140	141	Ave.	s.d.
MgO	50.51	50.48	51.39	51.24	47.28	53.41	51.25	50.97	51.51	50.19	53.82	53.32	51.97	51.68	50.00	52.82	51.37	1.60
Al_2O_3	0.09	0.07	0.12	0.19	0.03	0.04	0.23	0.21	0.05	0.02	1.60	0.18	0.10	0.03	0.10	0.02		
SiO_2	39.73	40.38	40.3	39.26	39.63	38.96	40.01	40.84	41.01	40.49	40.09	40.78	40.77	36.48	37.25	39.86	39.55	1.49
CaO	0.09	0.08	0.07	0.04	0.11	bdl	0.09	0.05	bdl	0.05	bdl	bdl	0.05	0	bdl	0.07		
FeO	10.78	9.39	7.92	7.52	7.45	11.11	8.96	8.73	7.59	9.72	5.02	7.09	7.53	18.58	15.09	9.09	9.47	3.30
MnO	0.12	0.17	0.11	0.17	0.12	0.11	0.1	0.12	0.12	0.14	0.11	0.08	0.14	0.13	bdl	0.09		
Total	101.4	100.6	99.91	98.46	91.69	103.7	100.7	100.9	100.3	100.7	100.7	101.5	100.6	106.9	102.6	102.1		
Mg#	Fo89	Fo90	Fo92	Fo92	Fo92	Fo89	Fo91	Fo91	Fo92	Fo90	Fo95	Fo93	Fo92	Fo83	Fo85	Fo91		

Results are given in wt-%. Analyses obtained from fractures can lead to totals below 100. Those exceeding 100 were likely caused by iron being present as metal. a) Spot analyses of fractured and undulose grains show no significant variation in major elements. The Mg number (Mg#) remains stable between Fo92 and Fo91 for most analyses consistent with San Carlos olivine. b) Spot analyses within the RA area, where two immiscible melts cooled show a stronger variation across major elements. FeO values vary between 5.02 wt-% and 18.58 wt-% and the associated Mg# varies from Fo83 to Fo92. Analyses with high FeO values and low Mg # suggest sites where iron was not only incorporated into the forming olivine, but also aggregated in metal blebs. Average (ave.) values and the associated standard deviation (1 s) are given for major elements.

6

and Rhodonite (MnO).

2.6. Raman spectroscopy We performed Raman spectroscopy in sample areas with higher Fe^0 metal droplet abundances to discern whether the surrounding silicate groundmass was rendered amorphous or retained its crystalline nature. Raman measurements were made with an Ocean Optics IDR-Micro Raman system (IRIS laboratory, Münster) using a OneFocus optical system with a 40× objective. The laser operates at 532 nm and we used an excitation energy of 1.8 mW resulting in a spectral resolution of ~7 cm^{-1} and a spot size of approximately 2 μm. Power per area unit converts to ~0.6 mW μm^{-2} in our set-up. Five measurements (acquisition time 1 s each) were performed on the sample surface. Background and baseline were automatically subtracted. Spectral results of the shocked sample were compared with spectra derived from the crystal sleuth database (Laetsch and Downs, 2006). **3. Results**
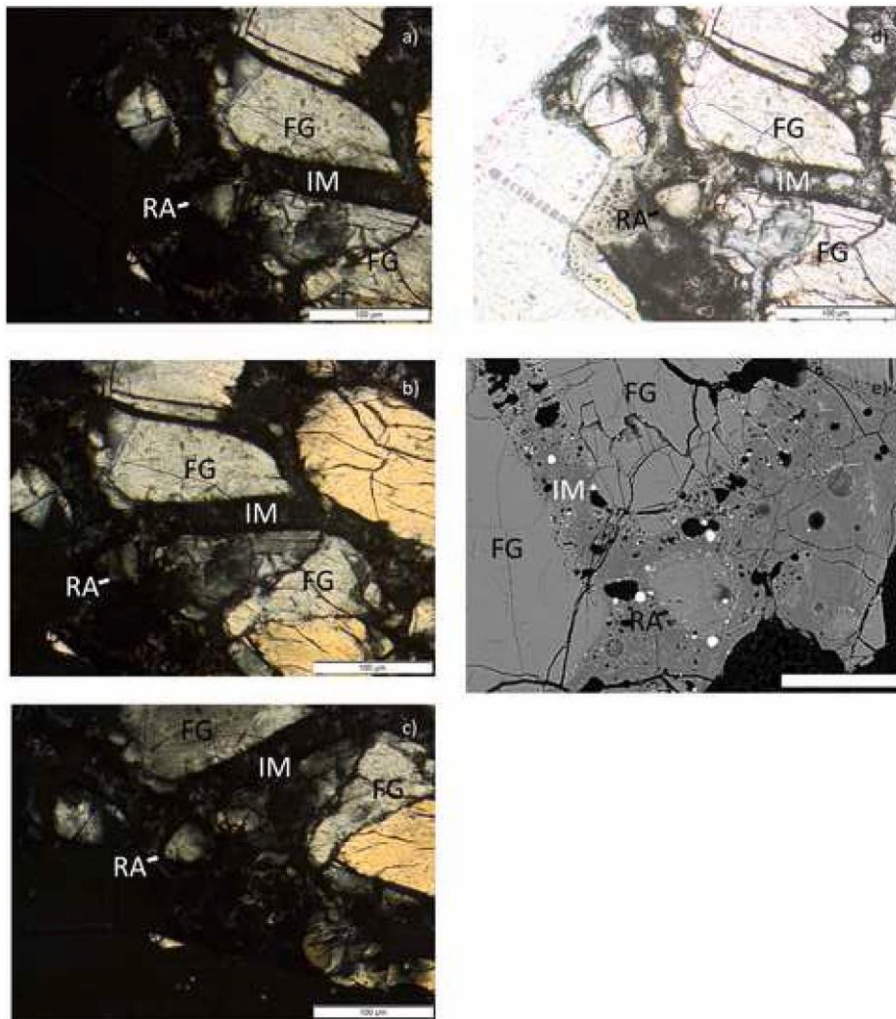
3.1. Optical microscopy and SEM

The sample represents unconsolidated (highly porous) ultramafic regolith material. The SEM SE overview micrograph (Fig. 2a) of the post-shock opened cylinder shows a compacted sample. The surface displays a highly variable topography, which was caused while retrieving the sample from the container and hints at a compaction gradient within the sample, e.g., strongly compacted areas can break out more easily if embedded in a matrix of less solidified material during sawing. A large fracture runs through the sample material parallel to the lower cylinder wall, also indicative of different compaction levels. The term lithology is not used in its geological definition sensu strictu, it rather denotes areas of similar pressure ranges and prominent features. In this regard, we distinguish three main "lithologies" in the corresponding thin section with the petrographic microscope (see outlined areas in Fig. 3a): L1) dark interstitial material with entrained grains, grain fragments, melt pockets and residual resin, L2) undulose grains and grains showing mosaicism, and L3) heavily and moderately fractured olivine grains comprising dense cumulate – like areas, in which some of the undulose grains and grains showing mosaicism are embedded. Observed melt pockets, undulose olivine grains and single olivine grains with mosaicism, as well as observed fractures suggest a shock classification according to the updated shock classification table (Stoffler et al., 2018¨) M − RE − S6. Natural rocks that suffered impact are categorized with this classification scheme; it has shortcomings when analogue material has to be classified by it. Rock classes (e.g., sediment, breccia, etc.) contain inherent information on porosity, rock comprising mineral species and grain size. The powder sample used for the experiment represents unconsolidated regolith material and the subgroup RE was chosen according to the updated scheme.

3.2. EPMA

Quantitative analyses of relevant areas (recrystallized area, undulose grains, and grains showing mosaicism etc.) yield results that do not show a strong variation from the respective average concentration in major element analyses (FeO, SiO_2, and MgO) in the undulose grain area. The results are consistent with typical San Carlos olivine (Table 1a). Results for MgO vary only moderately from the averaged analyses (51.60 wt% ± 0.99 wt%), for FeO the standard deviation (8.52 wt% ± 0.39 wt%) is slightly lower and it is very small for SiO_2 (40.80 wt% ± 0.11 wt%).

Variations within a patch termed recrystallized area (RA) are strong for the MgO and SiO_2 concentrations (51.37 wt% ± 1.60 wt% and 39.55 wt% ± 1.49 wt% respectively), and strongest in the FeO results (9.47 wt % ± 3.30 wt%). Contamination by liquefied parts of the surrounding ARMCO-Fe cylinder is likely responsible for the occasionally massive
local enhancement of iron. However, known shock features in many meteorites involve the formation of Fe, Ni droplets and/or troilite within the crystalline silicate groundmass (e.g., Rubin, 1992). Although the sizes and distribution of Fe^0 metal particles suggest that most of them were formed by contamination from the sample container, their location within the silicate

groundmass (see bright specks in dark matrix in Fig. 2a) makes them interesting for remote sensing analyses as explained in Section 4.1.

Analyses with totals below 100% stem from fragmented grain areas and/or areas with residual resin and few entrained Fe⁰ metal particles. Totals exceeding 100 are indicative of a metal fraction being present. Table 1a and b show the calculated Mg number, which do not vary in a (Fo92 to Fo91) but show strong variation in b, the RA area (Fo83 to Fo95).

3.3. FTIR results

3.3.1. L1: Dark interstitial material with entrained grains, grain fragments, and residual resin

L1 consists of dark interstitial material, fractured grains (FG) (see FG, Fig. 4a–e) and a melt/RA portion. The interstitial material (IM) is a mixture of residual resin mixed with parts of the finest olivine fraction and Fe-metal intrusions from the ARMCO Fe - cylinder.

The spectra obtained from both areas, marked as RA and FG in Fig. 4a, show dominant olivine typical features (Servoin and Piriou, 1973, Iishi 1978) shown in Fig. 5a and b. They range between 1040 cm⁻¹ and 1017 cm⁻¹ (9.6 μm – 9.8 μm) for RB1, not a genuine fundamental vibration of the orthosilicate ion in the olivine structure, rather an overtone (Hofmeister, 1987, Reynard, 1991, Hofmeister, 1997), 983 cm⁻¹ - 979 cm⁻¹ (10.2 μm) for RB2, and 937 cm⁻¹–892 cm⁻¹ (10.7 μm – 11.2 μm) for RB3, and 850 cm⁻¹–839 cm⁻¹ (11.8 μm – 11.9 μm) for RB4 in the RA (Fig. 5a), and 1056 cm⁻¹–1025 cm⁻¹ (9.5 μm – 9.8 μm) for RB1, 983 cm⁻¹ - 979 cm⁻¹ (10.2 μm) for RB2, and 945 cm⁻¹ - 905 cm⁻¹

(10.6 μm – 11.1 μm) for RB3, and 838 cm⁻¹–804 cm⁻¹ (11.9 μm – 12.4 μm) for RB4 in the FG area in Fig. 5b. The CF between recrystallized and fragmented grain areas did not shift for most spectra (CF ≈ 1117 cm⁻¹ (9.0 μm)). However, we can distinguish two CF positions within the RA area. In spectra in which the combination band RB1 is almost completely absent, the position of the CF shifts toward lower wavenumbers (≈ 1090 cm⁻¹ (9.2 μm)); in spectra with significant RB1, the CF is located at 1117 cm⁻¹ (9.0 μm). Furthermore, an additional very weak peak before the combination band is observed at ≈ 1095 cm⁻¹ (9.1 μm). This peak also occurs in selected spectra from grains embedded in the L1 area (arrows point at weak band in spectra displayed in Fig. 9b).

3.3.2. L2 undulose grains and grains showing mosaicism

A large undulose grain (long axis = 380 μm) shows the onset of mosaicism (mottled appearance of extinction) and two sets of nearly orthogonal fractures (Fig. 6a–e), which agrees with shock stage S4 (Stoffler et al., 2019¨). The corresponding spectra in Fig. 7 display bands that are typical for forsteritic olivine (Hofmeister, 1987; Reynard, 1991).

The reflectance minimum located between RB2 at 980 cm⁻¹ (10.2 μm), a

Fig. 4. a – c) Crossed polarized light images taken at different angles a) 0°, b) 35°, c) 60°). Image shows section of area labelled L1 in Fig. 3a and contains different building blocks – a recrystallized area (RA – see Section 3.2 for details), interstitial material (IM – see Section 3.1 for details) and fractured grains (FGs). The RA (white arrow) shows a moving extinction band within the confines of RA probably indicative of submicron sized olivine crystals comprising this patch. The corresponding plane polarized light image is shown in d) and shows large, fractured grains cross-cut by interstitial material. e) shows the corresponding EPMA back scattered electron (BSE) micrograph of the area. Bright circular features are liquid Fe⁰ - intrusions from the surrounding cylinder. The RA – labelled area denotes an area derived from a metal and silicate-rich melt; now showing recrystallized olivine and Fe⁰-metal features. Spectra shown in Fig. 5a and b were extracted from areas marked as recrystallized (RA) and fractured grain (FG) areas. Scale bar is 100 μm in a) to d) and 50 μm in e).
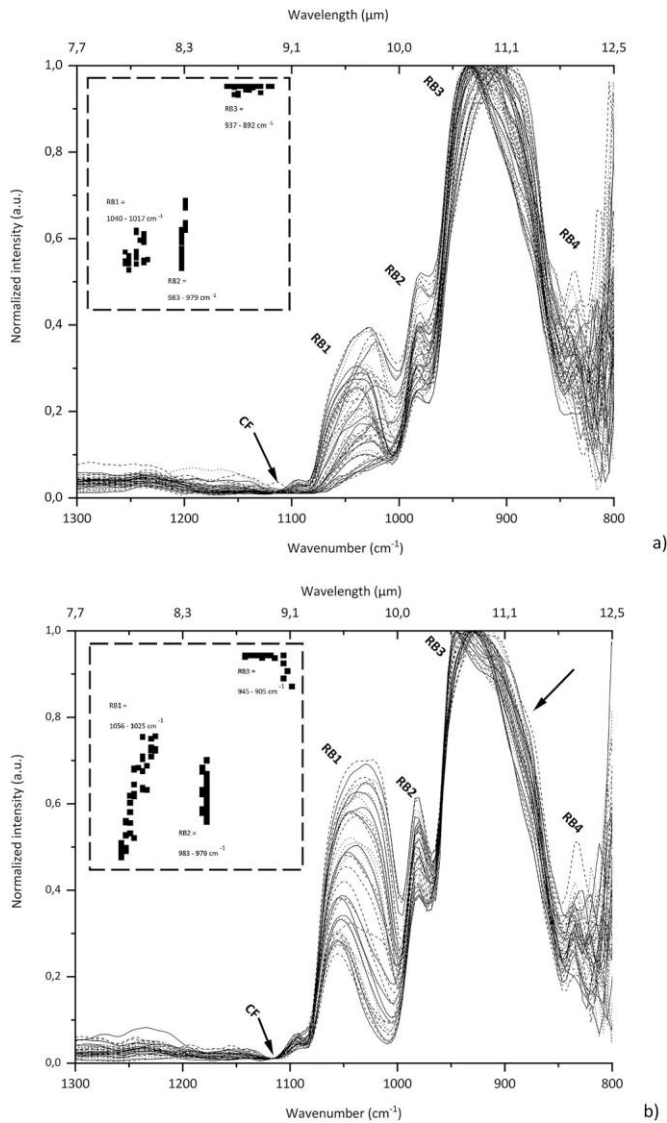
Fig. 5. Min/max normalized spectra extracted RA and FG labelled areas in Fig. 4a). The energy of fundamental vibrations is given in wavenumbers (cm^{-1}, lower abscissa) as well as wavelength (μm, upper abscissa). a) Depicted are 58 spot measurements from the RA area. The CF is located at ~1117 cm^{-1}. Average values for the strongest RBs and their respective standard deviation

(sd) are RB1 at 1030 cm^{-1} (sd = 6), RB2 at 982 cm^{-1} (sd = 2), and RB3 at 907 cm^{-1} (sd = 13). Note that RB1 is in some spectra completely absent, probably due to newly crystallized minute olivine crystals, cracks, melt or larger metal fractions. Peak center distribution diagrams are inset in a) and b) showing the spread of the maxima of the strongest RB in both areas.

b) Min/max normalized spectra extracted from the white outlined area marked as FG. Depicted are 42 spot measurements. The CF is located at ~1117 cm^{-1}. Average values for the strongest RBs and their respective standard deviation

(sd) are RB1 at 1043 cm^{-1} (sd = 10), RB2 at 981 cm^{-1} (sd = 2), and RB3 at 931 cm^{-1} (sd = 11). Note that RB3 has an additional shoulder (black arrow) in 26 out of 42 spectra.

band that shows the least frequency spread, and RB3 ≈ 926 cm^{-1} (10.8 μm) is attenuated in most of the spectra. Fundamental features, e.g., the CF occur at 1086 cm^{-1} (9.2 μm), RB1 ≈ 1060 cm^{-1} (9.4 μm), RB2 at 980 cm^{-1} (10.2 μm), RB3 between 926 cm^{-1} and 875 cm^{-1} (10.8 μm – 11.4 μm), and RB4 between 842 cm^{-1} and 804 cm^{-1} (11.9 μm – 12.4 μm).

3.3.3. L3 cumulate area

L3 is a cumulate – like area, characterized by tightly packed grains, most of them showing fractures (corresponding to shock stage S1), and some displaying more advanced stages of shock (e.g., undulose grains

(corresponding to shock stage S2), two grains showing mosaicism (corresponding to shock stage S4). Shock stages in this area are best represented by the categories S1 – S4 based on the features visible in the petrographic microscope. L3 does not contain dark interstitial material to the extent seen in the area described in 3.3.1. IM – like material only shows as thin dark lines between some of the larger grains, if at all. Reflectance spectra were obtained from grains enclosed in the area labelled L3 in Fig. 3a. An average spectrum out of 529 spectra was obtained and is shown in Fig. 11e. The CF is located at 1094 cm^{-1} (9.1 μm), significant RBs show at 980 cm^{-1} (10.2 μm), and 922 cm^{-1} (10.9 μm), and a combination band at 1056 cm^{-1} (9.5 μm). In contrast to spectra obtained from single fragmented grains and some of the spectra displayed in RA area in Fig. 5a, the CF shifted ≈ 20 cm^{-1} (0.2 μm).

4. Discussion

The sample shows distinct shock and peak temperature stages as inferred from microscopic observations. Observed shock features (melt/recrystallization area, grains displaying mosaicism, undulose grains, and planar fractures, see Figs. 3, 4, and 6 are indicative of a pressure range up to 60 GPa (Stoffler et al., 1991¨ , 2018, 2019). Post-shock heating locally led to a significant temperature rise as inferred from partially molten interface (cylinder/sample) areas.

Owing to the relatively wide range of the P, T – distribution within the run-product, clues on distinct planetary settings are possible with caution.

4.1. L1: RA, iron intrusion, agglutinate formation and resemblance to shock effects in porous chondritic material

4.1.1. RA and iron intrusion

Cooling patterns of two melts, one silicate – rich and one iron – enriched melt, led to microscopic Fe^0 metal blebs embedded in a silicate matrix (Fig. 8). Fig. 8 shows that pressure combined with impedance heating from crushed pore space were locally sufficient to melt forsteritic olivine (T$_m$ ~ 1890 °C) (for pore space reduction and impedance heating, see Güldemeister et al., 2013). Chemical analyses (Table 1b) show moderate chemical evidence for a Mg – enrichment, rather locally restricted Mg-spikes in single measurements (Fo$_{98}$, Fo$_{95}$, etc.) than uniform systematic enrichments of the entire RA, and the newly crystallized olivine grains contained therein. The RA represents quenched melt with distributed Fe^0 that was expelled from the melted progenitor olivine and additional iron that was mobilized upon impact from the surrounding container. Yet, the associated FTIR data from the RA lack systematic shifts including RBs and CFs toward longer wavenumbers (= shorter wavelengths), as these shifts are typically associated with an FeO depletion in silicates. An effect that could be attributed either to diffraction effects occurring in μ-FTIR (Sandt et al., 2019) or on the other hand could imply that moderate Mg/Fe – ratio variations (2–5 mol% Fo) in areas where olivine is a rock-forming mineral, e.g., high-Mg, high-Mg North Terrane and the Rachmaninov Basin on Mercury (Peplowski and Stockstill-Cahill, 2019) would possibly be difficult to detect in the MIR (for systematic Mg/Fe variation in olivine, see also Hamilton, 2010). Observed spectral differences, when the average RA spectrum and the unshocked SC database reference olivine spectrum (Fig. 12a and f) are compared, are not significant and do not indicate a composition-related shift, e.g., RB3 shifts about ~15 cm^{-1} (corresponds to ~0.15 μm) toward shorter wavenumbers and this would be indicative of an Fe-enrichment rather than depletion (see e.g., Salisbury et al., 1991).

4.1.2. How would agglutinates look like in a Hermean environment?

The RA area is also optically remarkable. It shows a distinct extinction feature, a slightly curved thin diagonal moving across the RA under cross polarized light at a 45° angle with respect to the viewing plane and the sample surface (white arrow in Fig. 4a–c). This can be indicative of micron - and
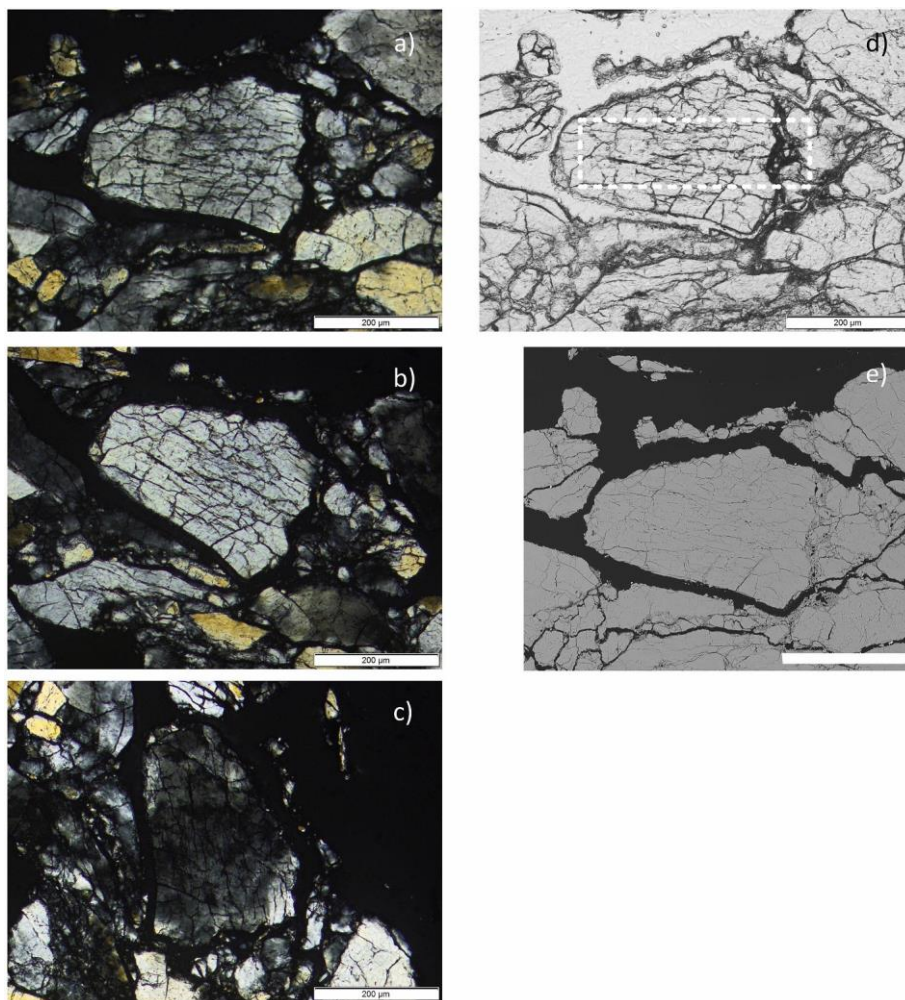
show the most intense RB caused by its Si-tetrahedra molecular vibrations than weaker fundamental vibrations caused by other cation – oxygen bonds. The spectra that we obtained from the RA vary in appearance, as the melt patch indeed shows moderate chemical heterogeneity (Table 1b). Spectral

Fig. 6. Cross polarized micrographs of undulose extincting grain at different angles shown in a) – c). White dashed rectangle in the parallel polarized light image (d)) denotes area from which spectral information were retrieved. Grain also shows two sets of fractures. Scale bar is 200 μm. e) BSE micrograph shows crosscutting crack separating the grain in two distinct parts, a part of which the right sight side fragmented into smaller subgrains.

submicron-sized olivine crystals that were quenched from the melt. In the lunar environment agglutinates are aggregates of crystals fused in a glassy matrix or are completely glassy specimen containing $npFe^0$ and microscopic Fe^0 that are produced during (micro) - meteorite impacts (Pieters and Taylor, 2003; Vance et al., 2016). Meanwhile, the composition of the glassy matrix seems to strongly depend on the impacted terranes from which the local regolith formed (e.g., Walker and Papike, 1982). According to calculations proposed by Cintala, 1992, 1993), the meteorite flux at mercury is 5.5 times higher than that at the Moon and the melt production rate in one microcrater event is 2.6 times higher than in a comparable lunar event. FTIR measurements of lunar glasses of different areas show one dominant RB in the range between 1000 cm^{-1} and 900 cm^{-1} (10 μm and 11.1 μm) (Zeng et al., 2019). Many investigated glasses, all SiO_2-rich, show a rather featureless appearance in the investigated spectral range, regardless of their initial chemical composition. Although glasses do not possess a far range order, complex SiO_4 - tetrahedra are the main constituent, all of which are connected to surrounding cations to varying degrees. This is giving rise to varying degrees of near and intermediate range order. The onset of structural organization is resulting in spectra with RBs occurring in the range between 1050 cm^{-1} and 850 cm^{-1} (9.5 μm – 11.8 μm) that are mainly caused by molecular vibrations within the orthosilicate anion. The broad peak between 1000 cm^{-1} and 900 cm^{-1} (10 μm – 11.1 μm) in this study is the strongest and it seems plausible that a glass would more likely

wise cumulative single spot measurements from the same area (Fig. 5a) show a variation of an overtone located at 1030 cm^{-1} ($\approx$ 9.7 μm) that is probably related to the chemical heterogeneity, and decreased relative intensities among the RBs (Figs. 5a, and 12a). High day time temperatures prevailing on Mercury's surface and the continuous influx of solar particles, would probably devitrify large parts of the amorphous agglutinates on Mercury's surface over time, which would result in an aggregate of glassy matrix, crystals, and npFe0 (Lucey and Riner, 2011 and references therein).

Thus, spectra obtained from the RA area can represent a stadium of agglutinate formation in a hot Hermean surface environment.

4.1.3. Extended L1 area and its resemblance to shocked porous chondritic material

The (sub) microscopic Fe^0 metal in the L1 area of the sample (Figs. 3a and 4e) is predominantly attributed to contamination processes from the surrounding ARMCO FE cylinder, which encased the powder sample during impact. The locally restricted massive intrusion of Fe^0 from the container material aggregated in large blebs spreading along previously existing grain boundaries. However, although unintended, the addition of the Fe^0 derived from the ARMCO cylinder produced analog material that, with some restrictions, resembles porous shocked chondritic
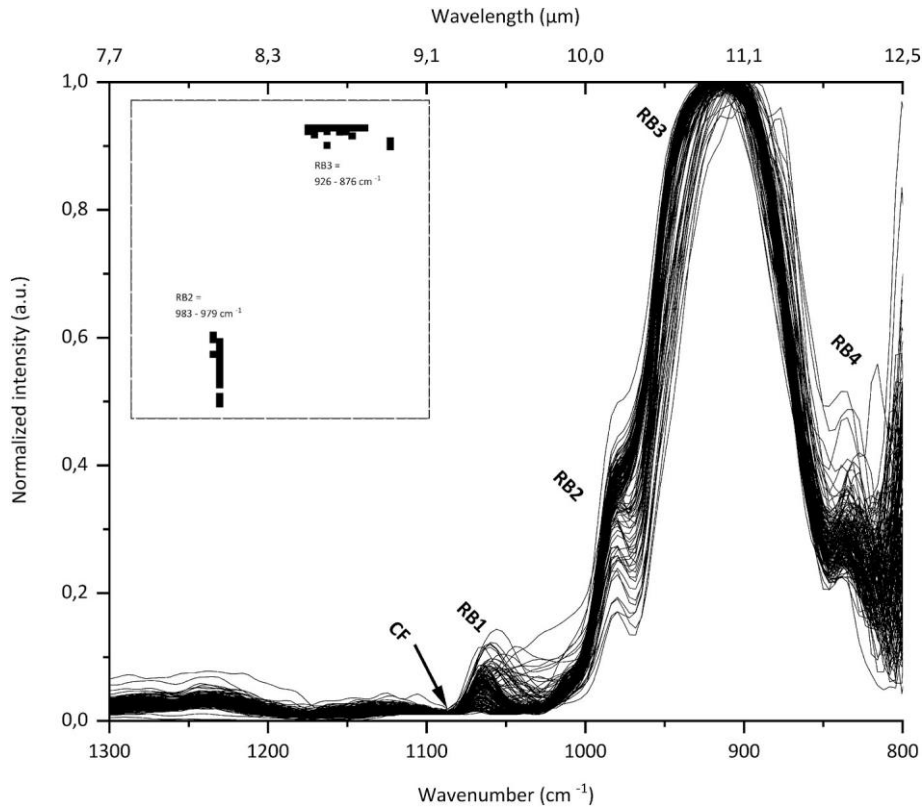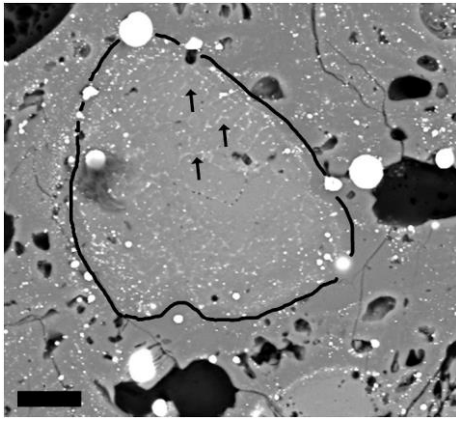
veins, dikes, and blebs, form upon varying degrees of impact shock. A recent experimental study showed varying shock stages in situ within the same sample portion of the Chelyabinsk meteorite (Kohout et al., 2020). In the higher shock regimes, this vein formation leads to optical darkening, i. e., shock darkening (e.g., Britt and Pieters, 1994, Van der Bogert et al., 2003, Kohout et al., 2014).

However, the overall decrease in intensity that is associated with Fe^0 bleb areas in the entire L1 area (Fig. 9a–b) is rather comparable to experiments conducted by Hirata et al. (2009) and its implications for porous metal and silicate materials. The metal blebs formed by local T excursions due to crushed pore space and were transported along existing interstitial cavities between grains, which does not require the high shock pressures that are necessary for the mobilization and re- distribution of metal and metal sulfide veins across compact ordinary chondrites. The spectra associated with the iron dominated blebs in Fig. 9a and b could therefore represent spectra that can be compared

Fig. 7. Depicted are 160 spectra associated with the outlined area in Fig. 6d). 160 spectra were analyzed to determine the spread of the band maxima (inset diagram). The CF is located at 1086 cm^{-1}, RBs follow at 1060 cm^{-1}, 980 cm^{-1}, 926–875 cm^{-1}, and 842–804 cm^{-1}.

Fig. 8. EPMA BSE image. Bright patterns (Fe metal, see Table 1) within darker silicate matrix in L1 area are cooling patterns that formed from a metal- enriched melt and a silicate-rich melt. Arrows point at locations where cooling textures of the metal − enriched phase form peculiar patterns within a re- crystallized silicate matrix Scale bar is 10 μm.

to naturally shocked porous chondrites.

Although not directly comparable in terms of sample and pattern provenance, the L1 area from this study shows a similar loss of spectral features that is described by Morlok et al. (2017) (see Fig. 8 therein) in the shock-darkened "lithology" of the Chelyabinsk chondrite. The described loss

material. Restrictions are mainly set by the lack of mineral diversity in this study. However, although chondritic material has a distinct mineral composition, a comparison between spectral information of the L1 area and porous shocked chondritic material in terms of the mobilized metal fraction and its impact on the spectral information of the surrounding shocked silicates seems valid. Hirata et al. (2009) performed impact experiments on porous analog material at different impact pressures (20 GPa − 70 GPa). Similar patterns regarding metal bleb formation and silicate compaction, as well as melting were obtained in a pressure range between 30.8 GPa and 43.6 GPa (see Figs. 4a and 8 in Hirata (2009)). Shock darkening involves the mobilization of metal sulfides, metal oxides and/or metal alloy blebs (Rubin, 1992). Metal alloys and metal sulfides are comprising phases in most unequilibrated ordinary chondrites, and owing to the ductile behavior of metals, metal alloys,

of the spectral twin peak feature between 10.8 μm and 11.3 μm (926 cm^{-1}– 885 cm^{-1}) in the meteorite is similar to what we see in spectra from the RA (dominant olivine matrix with dispersed small metal particles) and those spectra obtained strictly from larger iron blebs. Spectra from both areas display one broadened band between 960 cm^{-1} and 850 cm^{-1} (10.4 μm and 11.8 μm) instead of two distinct peaks in this range. It could be argued that this is related to orientation effects (see fig. 5 in Reynard, 1991 for more detail), and this could apply to the olivine dominant spectra of the RA. However, this seems unlikely
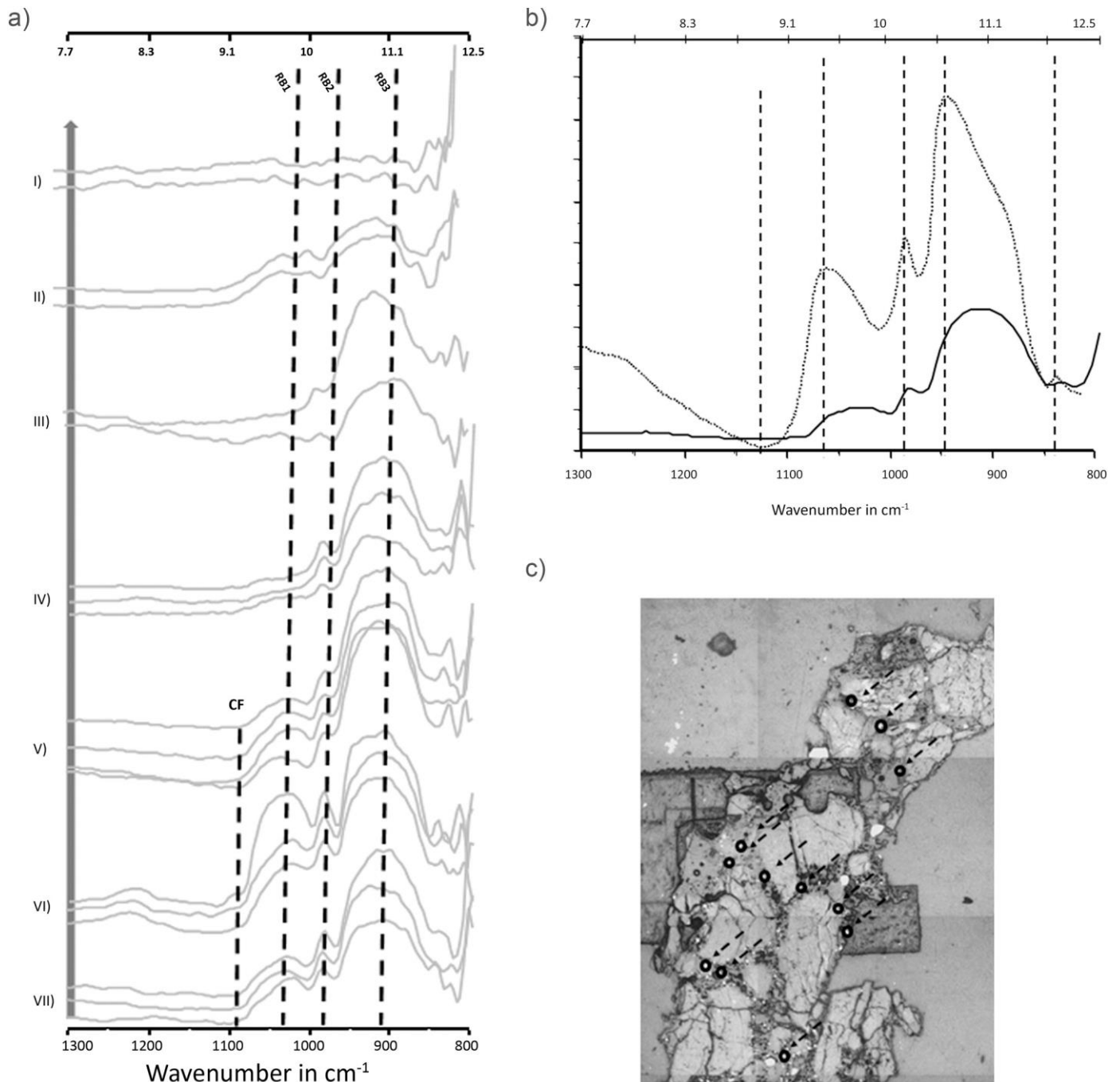
Fig. 9. a) Reflectance spectra shown in this figure were obtained from iron (Fe^0 _metal) spots dispersed within the interstitial material between grains. Black circles and arrows in the incident light image (c)) show exact locations from which the measurements were obtained. Only spectra from those spots contributed, of which the diameter was a minimum of ~10 μm, so that measurements located in the center of the metal spot were available, rather than those from margins or metal/silicate interfaces. Dashed lines mark the most important features in the spectra, the CF (~1117 cm^{-1} where it could be identified), and the typical bands expected for olivine. RBs are located at ~1030 cm^{-1}, 980 cm^{-1}, and between ~940 cm^{-1} 895 cm^{-1}. Spectral contrast is attenuated in the spectra labelled I), II), III) and IV). Olivine - like features show in spectra from V) to VII). All spectra were offset for clarity and were not normalized according to their Min/Max intensity. In total, 92 measurements were obtained from iron metal sites within the sample; the resulting average spectrum is displayed in b) where the CF is slightly shifted toward shorter wavenumbers and the baseline is enhanced. Olivine typical features are prominent and show at ~1040 cm^{-1}, 979 cm^{-1} and ~ 930 cm^{-1} and an additional band at ~840 cm^{-1}. Dashed line in graph is a diffuse reflectance spectrum obtained from the unshocked and ground source olivine for comparison of olivine RB locations. Arrow to the left in Fig. 9a) indicates increasing Fe-contribution to the signal. c) Incident light image with black circles and arrows showing the position of the iron blebs, which appear bright in this image as they reflect the incident light stronger than the surrounding silicate material. Scale bar is 500 μm.

for the metal dominated spectra of the iron bleb spot measurements (Fig. 9a and b). For comparison, the unshocked olivine (dashed line in Fig. 9b) shows a prominent peak at 940 cm^{-1} (10.6 μm) and a shoulder at ~875 cm^{-1} (11.4 μm), the latter of which is completely absent in the average iron bleb spectrum (solid line), which instead displays a

broadened and plateau-shaped band. Furthermore, the RA spectra (Fig. 5a) also lack the shoulder at 875 cm^{-1} (11.4 μm) that occurs in most of the spectra derived from nearby fragmented grains (Fig. 5b), which could be indicative of a genuine shock process involved rather than an orientation effect. However, at this point orientation effects cannot be ruled out completely.

In general, spectra obtained from metal blebs dispersed within the interstitial material and olivine grains range from attenuated low contrast

spectra (see Fig. 9a, specifically spectral groups I, II, and III) to predominantly olivine – like spectra (spectral groups *V* - VII; IV seems to resemble an intermediate stage). However, in contrast to spectra obtained from genuine unshocked SC olivines (dashed line), the CF in the average metal bleb spectra is shifted to shorter wavenumbers (CF $\sim$ 1090 cm^{-1} (9.2 μm)), which would indicate a more fayalitic endmember (for mid-infrared spectra comparing fayalitic and forsteritic olivine endmembers, see Hofmeister, 1987, Hamilton, 2010, Lane et al., 2011). However, comparing spectral CF locations from diffuse and specular reflectance spectra can introduce flaws in interpretations based solely on the spectral location of the CF, as lattice overtones in the spectral range between 1800 cm^{-1} and 1400 cm^{-1} ($\sim$ 5.5 μm - $\sim$7 μm) are virtually non-existent in the specular mode. Hence, an intensity minimum is difficult to determine accurately. Although these spectra were obtained strictly from large metal blebs, olivine spectral features are obviously dominant. Why spectral features of olivine occur in spectra obtained from iron particles can either be explained by a slight offset of the measurement spots on the sample surface resulting in the measurement of interface areas (silicate/metal), by diffraction effects caused by overlapping pixels (Sandt et al., 2019, or as genuine metal spectra seem to be rather featureless in the 1300 cm^{-1}–800 cm^{-1} (7.7 μm – 12.5 μm) range, only a small amount of olivine surface would be sufficient to give rise to relatively strong olivine features. The latter seems to be plausible when the quality of the spectra in Fig. 9a) is compared to dedicated olivine spectra.

However, iron blebs seem to have an attenuating effect on the resulting composite spectrum in the mid-infrared range, and the baseline also seems slightly enhanced.

4.2. L2: grains showing mosaicism, undulose grains (L2) embedded in L1: orientation effects, stable RBs, and overtones

Grains displaying fractures, undulose extinction or mosaicism show distinct spectra, when compared to each other (Fig. 10a and b). All selected grains show fractures, but not all suffered enough impact pressure to display mosaicism or undulose extinction. However, similarities between overall spectral shapes are obvious and spectra associated with grains 6, 10, and to a lesser extent grain 1, can be placed into one subgroup showing a strongly attenuated RB2 and a broad RB3. This subgroup is probably related to what is described by Reynard (1991) as a mixed orientation B1u(B3u) and is not the result of the previously suffered impact pressure as stated by Martin et al. (2017). Also, spectra of grains 2, 3, 5, 7, 8, and 9 are probably indicative of an orientation effect (see Fig. 1 (B3u) in Hofmeister (1987)). Spectra related to grains 1 and 4 show a rounded broad band rather than a sharp peak between 960 and 850 cm^{-1} (10.4 μm and 11.8 μm). This probably cannot be explained by orientation-related effects only and is possibly linked to iron particles being present (same rounded and broadened shape can be seen in Fig. 9b). An average spectrum (dashed line in Fig. 11) obtained from all grains discussed here (see Fig. 10 for detailed spectra) is comparable to spectra obtained from the unshocked database olivine (grain size
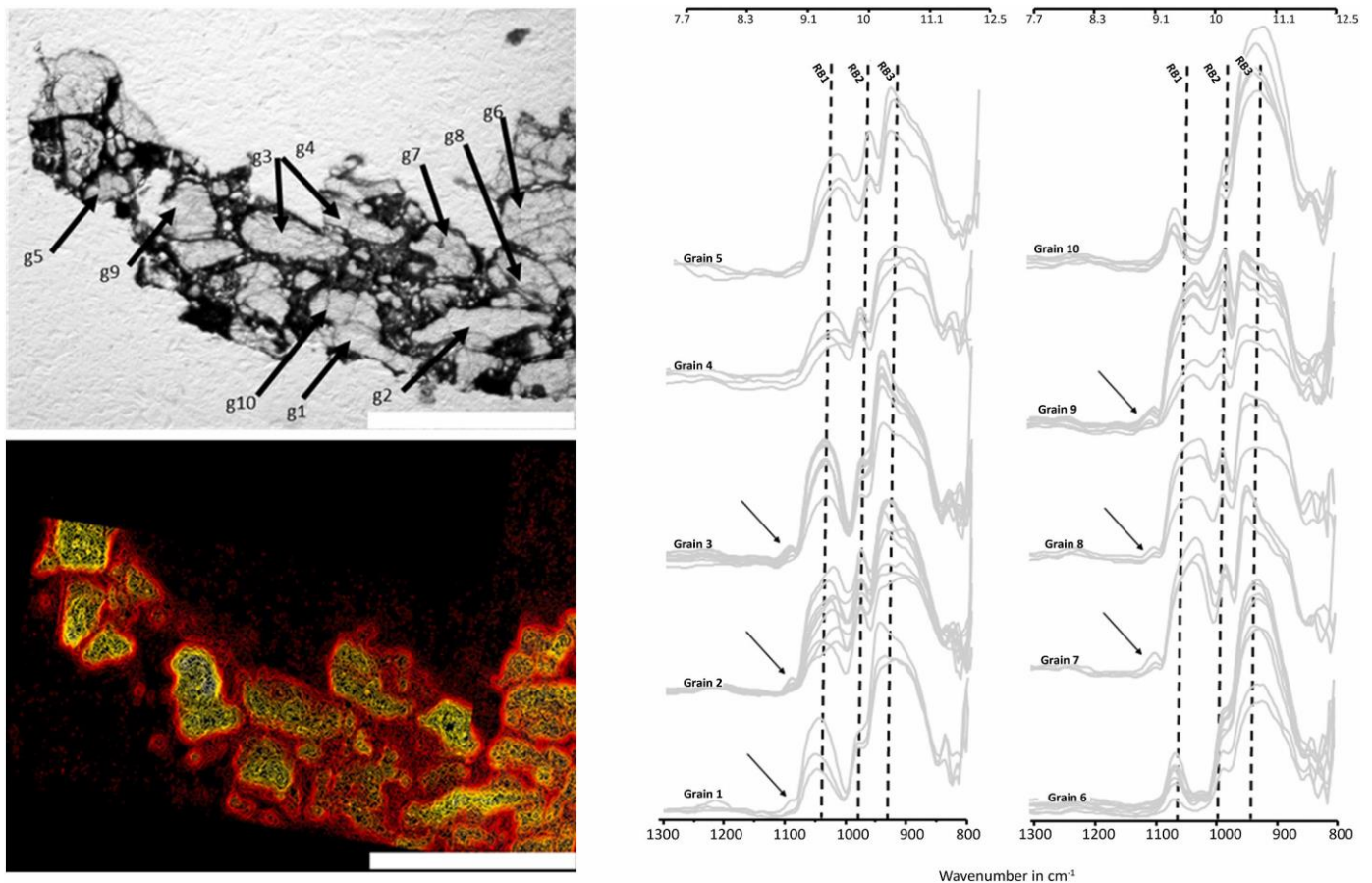

Fig. 10. Grains 1–10 are set in a matrix of L1 material that is mostly comprised of fractured and undulose grains (for details see Fig. 3a). The 2D μ-FTIR map over the intensity of RB2 shows the same portion of the sample. Scale bar is 500 μm. b) The most prominent olivine typical vibrational features are marked with dashed lines and are labelled RB1, RB2, and RB3 in all spectra. We abstained from normalizing the spectra according to their maximum. Several representative spectra from each grain were chosen. Some of the grains show an additional peak at ≈ 1100 cm^{-1} (black arrow in Grains 1, 2, 3, 7, 8, 9) which is completely absent in other spectra. In spectra where the pre-peak is present the CF occurs at approximately 1120 cm^{-1} ($\sim$ 8.9 μm), where it is absent the CF shifts to $\sim$1095 cm^{-1} (9.1 μm).
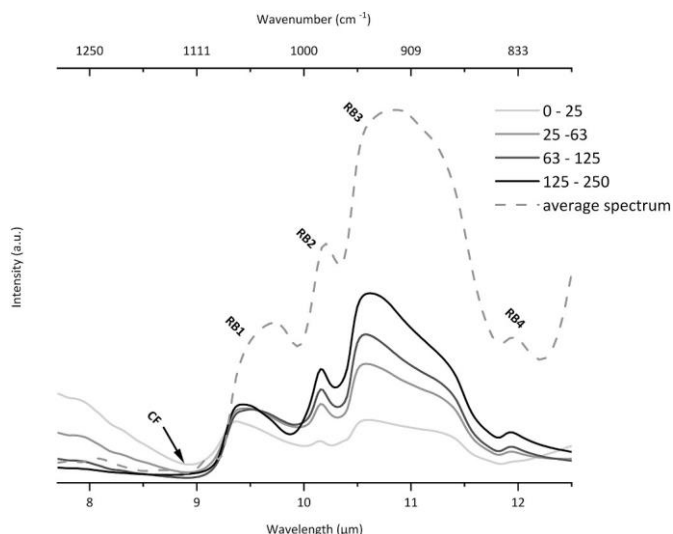
Fig. 11. Diffuse reflectance spectra obtained from sieved unshocked San Carlos olivine particulates (ID 187) that were obtained from the unshocked reference material compared to an average spectrum obtained from 115 spectra from the shocked olivine grains. The sieved particulates show a CF at ~1102 cm-1 (9.1 μm) and strong bands at 1060 cm-1 (9.4 μm), 983 cm-1 (10.2 μm), 942 cm-1 (10.6 μm) and a shoulder at ~870 cm-1 (11.5 μm). The inset average spectrum shows a weak band at 1102 cm-1 (9.1 μm), where the CF should be located and shows, compared to the sieved particulate a slightly shifted CF at 1118 cm-1 (8.9 μm).

fractions 25–250 μm in Fig. 11). In this case, diffuse reflectance spectra of different grain sizes from the database olivine are compared to the average spectrum obtained from grains 1–10 measured in specular reflectance mode. Differences in the spectral shape of the two main subgroups owing to distinct orientational effects (specular reflectance vs. diffuse reflectance) are cancelled out once the average spectrum is obtained, which envelopes the diffuse reflectance spectra of all grain size fractions. Average spectrum and diffuse reflectance spectra show bands at the same position (Fig. 11). This might allow the conclusion that if the average of the entirety of possible orientations in specular mode is obtained, the resulting average spectrum resembles a diffuse reflectance spectrum from the same area. Additionally, a weak peak at ~1100 cm^{-1} (9.1 μm) (black arrow in spectra in Fig. 10b) is observed in 6 out of 10 grains and is probably an overtone, which occurs in Fe-richer olivine endmembers in a B3u dominant polarization (see Table 1 in Hofmeister (1997)).

RB2 shows the least energy spread with the smallest standard deviation (see RB peak position spreads inset in Figs. 5a, b, and 7, which is observed throughout all acquired spectra in this study, regardless of orientation. It is a sharp narrow band; the stable position is likely the result of the stiffness of the bond that gives rise to this fundamental vibration. The narrow band shape could be indicative of a rather isolated position with no additional peripheral bonds that would otherwise cause a broadening of the normal mode (Siebert, 2013). All molecular vibrations in the RB region can be attributed to asymmetric stretching motions of the Si–O bonds of the SiO₄-tetrahedron. Calculated and experimentally observed normal mode frequencies for transverse and longitudinal optical waves of forsteritic olivine are given by Iishi (1978), Reynard (1991), Hofmeister (1987), and Noel et al., (2006). For example, the maximum of RB3 shifts significantly between 945 cm^{-1} and 892 cm^{-1} (10.6 μm and 11.2 μm) (range applies to both Fig. 5a and b), which could be related to the splitting of the longitudinal (LO) and transverse (TO) frequencies (ω_{TO} and ω_{LO}) of the optical wave in this range (see table 2 in Reynard (1991)), table 1 in Hofmeister (1997)).
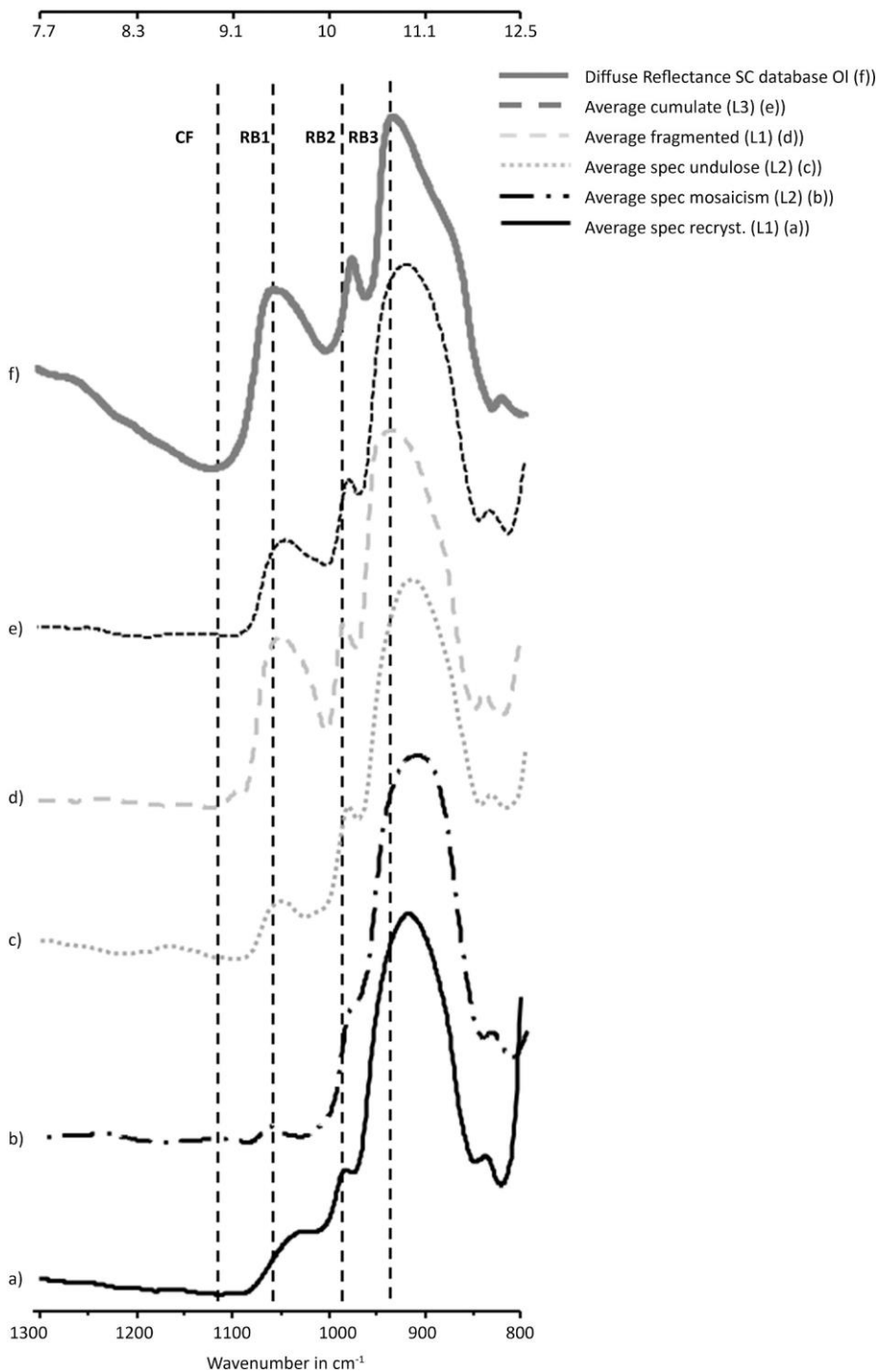
4.3. L1, L2, and L3: comparison of most prominent components in different "lithologies"

RB1, actually an overtone and not a fundamental vibrational mode, located at ~1060 cm^{-1} (9.4 μm) seems to be most susceptible to impact pressure or

gardening processes. In Fig. 12, average spectra of similar components and of specific areas derived from different "lithologies" within the sample are shown. A strongly attenuated and slightly shifted overtone is characteristic for the RA. This attenuated feature in the average spectrum is caused by many single measurement spectra exhibiting a completely subdued overtone in the source spectra. Spectra with subdued overtones also have attenuated RB2 and slightly broadened RB3 bands, which could either be indicative of a mixing of orientations or probably signifies the onset of crystallinity loss. The latter seems unlikely as most spectra can be explained by orientation effects. Raman spectra (Fig. 2b) obtained from locations most likely to host impact melt in the sample, if at all present, also show crystalline olivine typical spectra. The overtone at 1060 cm^{-1} (9.4 μm) increases gradually in intensity from RA (Fig. 12a), mosaicism − grains (Fig. 12b), undulose extincting grains (Fig. 12c), fragmented grains (Fig. 12d), dense cumulate grains (L3 area), and the average spectrum of the database olivine (Fig. 12f). Gardening of a regolith layer could also lead to a change of orientation - dependent effects within the reflectance spectrum. Positions of genuine RBs are moderately (RB3) or not at all affected (RB2). An observed shift of the CF is caused by averaging over spectra with slightly different properties (some of them having the additional band at ~1100 cm^{-1} (9.1 μm) and some not). This leads to an averaged spectrum that shows no band at 1100 cm^{-1} (9.1 μm), the lack of which shifts the CF toward 1095 cm^{-1} (9.1 μm) rather than 1117 cm^{-1} (9.0 μm) as seen in Fig. 12d and f. A spectrum obtained by remote sensing techniques from a planetary surface will also be the result of an average spectrum of an entire area (several square kilometers) of heterogeneous material, which is why average spectra from the different "lithologies" were compared in Fig. 12. It seems that, especially in terms of shifted spectral features, we must be careful with respect to smaller or weaker bands. Their weak intensity might be cancelled out in an average spectrum, yet they have the potential to shift the position of the reflectance minimum (CF) and could therefore probably lead to false interpretations concerning the chemical composition.

4.4. Average spectra from large areas of L1, L2 and L3

Three spectra are shown in Fig. 13, each of which represents large areas within the confines of the respective "lithologies" L1, L2, and L3. L1 (blue) that consists of dark IM, fragmented grains, and presumably recrystallized olivine grains shows a typical olivine MIR spectrum. Differences are most pronounced when single components from these areas (see Fig. 12a and d) are compared to the average spectrum over the entirety of the components, e.g., L1 is comprised of fractured grains, and recrystallized areas. Yet, fundamental RBs do not shift and remain stable. L2 is an average spectrum derived from 9 grains that show different degrees of extinction anomalies between undulose extinction to mosaicism. Here, we see a broadening of RB3 that can be attributed to the development of a shoulder at ~890 cm^{-1} (11.2 μm). An unexpected feature is an additional peak at 1011 cm^{-1} (9.9 μm), for which we have no explanation. It seems to be closely related to the overtone located at 1040 cm^{-1} (9.6 μm). Regarding intensity, RB3 is darker in L3 than in L2, or L1. Its overtone located at 1029 cm^{-1} (9.7 μm) is the most intense, especially with respect to the L2 area. A weak peak occurs at ~1095 cm^{-1} (9.1 μm), which had been seen previously in the fraction of fragmented grains (see. Fig. 12e). The cumulate area chosen for the "lithology" overview is larger than that in Fig. 12 and more cracks in heavily fractured grains are present in the large overview. Overall, average spectra from distinct areas do not differ much, which is not surprising as the sample is monomineralic.

Fig. 12. a) An average spectrum from spectra of the silicate melt area RA are depicted in a). The CF shifts to shorter wavenumbers compared to spectra from Fig. 5a), which are spectra from the same area and the weak band at ≈1095 cm^{-1} (9.1 μm) is not visible in the average spectrum. The overtone band RB1, and the genuine fundamental vibrations RB2 and RB3 show at the same positions, as well as RB4. b) this average spectrum was derived from grains displaying mosaicism. Olivine typical combination and Reststrahlen bands are observed at ≈ 1055 cm^{-1} (9.5 μm), 980 cm^{-1} (10.2 μm) and 914 cm^{-1} (10.9 μm). The reflectance minimum between RB2 and RB3 is extremely shallow compared to other spectra. Also, the combination band at 1055 cm^{-1} (9.5 μm) is very weak. c) average spectrum derived from undulose extincting grains show similar features as displayed in b) with a slightly stronger combination band and a pronounced reflectance minimum between RB2 and RB3. d) is an average spectrum obtained from fragmented and fractured grains. A remnant of the weak peak at 1095 cm^{-1} (9.1 μm) can be observed shifting the CF to 1117 cm^{-1} (8.9 μm), a strong combination band at ≈ 1055 cm^{-1} (9.5 μm) and RB2 and RB3 are strongly pronounced, the latter being located at 940 cm^{-1}, which shifted slightly (∼ 15 cm^{-1}) when compared to spectra a) – c). e) The CF in the average spectrum derived from a large area of the cumulate area (see area L3 in Fig. 3a)) shows a CF at 1095 cm^{-1} (9.1 μm) a combination band at 1030 cm^{-1} (9.7 μm), RB2 at 979 cm^{-1} (10.2 μm) and RB3 at 914 cm^{-1} (10.9 μm). f) is the average spectrum derived from diffuse reflectance spectra of the database San Carlos olivine that was used throughout the experiment. It thus represents the unshocked stage. The CF is easier to locate in diffuse reflectance spectra as lattice overtones in the spectral range between 1300 cm^{-1} (7.7 μm) to 1110 cm^{-1} (9.0 μm), where the CF is approximately located in olivine, show higher intensity due to surface roughness. The reflectance minimum (CF) can therefore be easily identified. The specular reflectance spectra show an overall low intensity in this spectral range making it difficult to locate the exact position of the CF unambiguously.

4.5. L1: Spectral maps and parameterization for remote sensing and implications for Mercury

RB2 is an extremely stable fundamental vibration, virtually unaffected by orientation or impact related changes. A spectral map (Fig. 3b) was created by integrating over the intensity of the RB2 (more precisely the energy range between 985 cm^{-1}–978 cm^{-1} (10.2 μm)). Other olivine typical RBs and overtones show large spreads in their position and are therefore less suitable as a proxy for the presence of olivine within a given mineral mixture (on a planetary surface).

We could identify the location of an "alien" pyroxene grain within the thin section by producing a spectral map over the given wavenumber range. The pyroxene grain was incorporated accidentally, either during the preparation of the sample powder or had been attached to an olivine grain all along in the source rock from which the powder was then obtained. The location of the pyroxene grain appears black in the spectral map (white arrow in Fig. 3b) while the corresponding transmission light micrograph (Fig. 3a) shows the presence of sample material at this location, as opposed to a genuine void in the right half of the map, which is simply a hole as indicated by the corresponding area in Fig. 3a. Associated spectra from this particular grain showed that this grain indeed is pyroxene.

An important finding suggesting that the energy range of RB2 can probably be used as a proxy for the presence of olivine minerals within
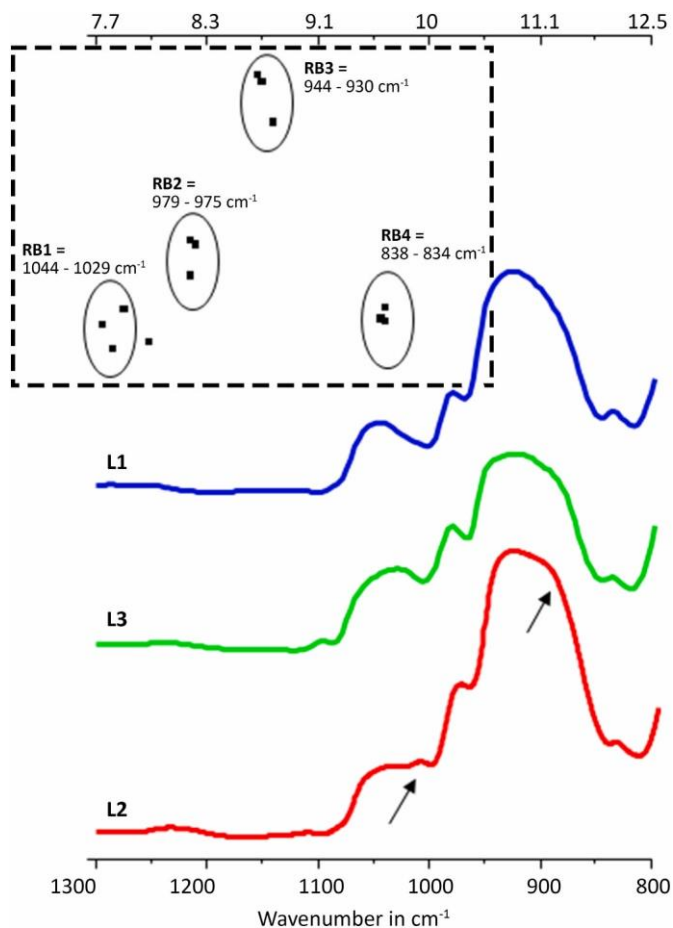
Fig. 13. Spectral comparison of lithologies: Overall intensities were not normalized and the spectra are offset for clarification.

They are average spectra of large areas that are representative for the respective categories.

To L1, three smaller areas, ~0.3 mm x 0.1 mm large, contributed to the signal, L2 was obtained from a total of 9 undulose grains and grains showing mosaicism, and L3 was obtained from an area ~ 1 mm × 0.6 mm large.

L1 is a mixture of dark interstitial material, fragmented and fractured grains, as well as recrystallized melt pockets, the CF occurs at 1097 cm^{-1} (9.1 µm), RB1 at 1044 cm^{-1} (9.6 µm), RB2 at 979 cm^{-1} (10.2 µm), RB3 at 926 cm^{-1} (10.8 µm) and RB4 at 835 cm^{-1} (12.0 µm).

L2 is an average spectrum obtained from 9 grains showing signs of shock (mosaicism is very common and even those grains labelled undulose extincting are in the stadium of 'onset of mosaicism'. The CF is located at 1096 cm^{-1} (9.1 µm), the RB1 at 1040 cm^{-1} (9.6 µm), a second peak (black arrow) is located between RB1 and RB2 at 1011 cm^{-1} (9.9 µm), RB2 at 979 cm^{-1} (10.2 µm), RB3 at 933 cm^{-1} (10.7 µm) and a shoulder (black arrow) at 896 cm^{-1}, RB4 is located at 835 cm^{-1} (12.0 µm).

L3 is mostly comprised of densely packed fractured grains and grains with higher shock signs. Veins are virtually absent. Its CF is located at 1117 cm^{-1} (8.9 µm), a weak peak is located at 1094 cm^{-1} (9.1 µm) before RB1, which is located at 1025 cm^{-1} (9.8 µm), RB2 occurs at 979 cm^{-1} (10.2 µm), RB3 at 926 cm^{-1} (10.8 µm) and probably a remnant of a shoulder at 888 cm^{-1} (11.3 µm), RB4 is stable and occurs at 835 cm^{-1} (12.0 µm).

A graph showing the spread of the respective RBs is inset. It is surprising that RB4 also remains very stable.

mineral mixtures. Spectral characteristics that are persistent in a multitude of different scenarios are important when remote sensing data are searched for spectral features indicative of composition or structural information.

In general, for the comparison of laboratory data with the expected results from MERTIS, we have to take several points into account. The spectral resolution of the laboratory measurements is an order of magnitude higher than that of the MERTIS spectrometer (0.02 µm vs. 0.2 µm) (Hiesinger et al., 2010). This has to be taken into account, when spectral features are compared.

Furthermore, the spatial resolution of the MERTIS instrument will be below 500 m only for 5–10% of the entire observation slot.

In any case, we expect an intricate mixture of many mineral and glass phases forming the Hermean planetary regolith, and for any model we will have to use several phases. The present study focuses only on one aspect of surface processing – space weathering.

Also, the ambient parameters that will be encountered on Mercury's surface, e.g., temperature, pressure, and porosity of the regolith will differ from the laboratory environment that we conduct our experiments in (Hiesinger et al., 2020).

5. Conclusion

We documented the spectral properties of shocked forsteritic olivine in the MIR range in detail in order to identify spectral features specific for this mineral that can be assigned to impact exposure as one branch of SW processes that change planetary surfaces over time. We started with a monomineralic sample in order to improve our understanding of how this mineral can contribute to mixtures. A future step will involve the detailed examination of mixing effects. In regard to olivine intrinsic spectral features in the MIR, the identified RB2 ($\approx$ 980 cm^{-1}) can probably serve as a proxy for the identification of olivine in spectra obtained from a diverse planetary regolith.

We found that minor shock stages, e.g., compaction processes and shock stages that involve the formation of mosaicism and undulose grains are probably invisible in the MIR and will be only of minor importance in this spectral range. Shock - induced distortions of the crystal lattice would be better visible in the far infrared region, a region in which lattice vibrations show and that is therefore more suitable for structural analyses than the molecular vibration region of the mid infrared range. However, this is valid only for a compacted surface. In a porous environment, e.g., a planetary regolith, where relatively low impact pressures lead to high temperature excursions due to impedance heating, we could identify melt production.

In an impact heated environment, we do see an intensity decrease due to the formation of smaller and bigger Fe^0 particles and the melting of the silicate phase. Furthermore, the particles likely also cause a peak broadening within the associated spectra that can also be attributed to a certain degree of non-crystalline silicate components still present.

The use of the micro-FTIR technique helped in identifying orientation effects in the olivine grains. Effects that were speculatively attributed to shock exposure by Martin et al. (2017) were identified as grain orientation effects and can help to improve our understanding of the diffuse reflectance spectra that statistically cover all possible grain orientations.

While not directly applicable to remote sensing data, the results presented here, will help to identify crucial parts in the MIR, which allow to gauge the effects of impact shock spectroscopically.

Declaration of Competing Interest None

declared.

Appendix

A.1. The CF and RBs in the MIR

The CF is a reflectance minimum or in the case of thermal emissivity spectra, a maximum in the midinfrared spectrum that occurs when the imaginary part of the refractive index (a term that considers the material specific dampening of a given electromagnetic wave within a medium) becomes negligible and the real part of the refractive index of the particulate sample equals that of the ambient air/vacuum. In other words, in the given frequency range, scattering of the incident wave is minimized and transmission for the respective wave frequency is maximized. Reflectance and

emissivity are connected via Kirchhoff's law $R = 1 - \varepsilon$ (R = reflectivity and ε = emissivity) a fundamental law that will be important in the light of a mission that will return thermal emission spectra from Mercury's surface. Reststrahlen bands (RBs) can be mainly attributed to fundamental transitions of internal molecular vibrations of the orthosilicate $-$ ion (the SiO_4- tetrahedron) typically occurring between $1180\ cm^{-1}$ and $830\ cm^{-1}$ (8.5 and 12 µm) for silicate mineral species. IR-allowed asymmetric, but also symmetric valence stretching modes of the Si−O bonds within the tetrahedron give rise to several silicate - species typical bands in the RB region. The eigenfrequency of the respective Si−O bonds resonates with matching frequencies of the incident electromagnetic wave. The bonds giving rise to the observed spectral signal are located within the surfaces of the irradiated crystal planes. At the same time the incident beam propagating into the crystal is attenuated strongly so that volume scattering is unlikely (except for very fine particles). For particles larger than the incoming wavelength, the RB region is dominantly a surface scattering area of the spectrum. The attenuation effect results mainly from the imaginary part of the refractive index, the extinction coefficient that becomes dominant affecting most of the frequency range of the incoming wave. Although the intensity of RBs can vary, their intensity in one spot analysis is cross correlated.

References

Benkhoff, J., Van Casteren, J., Hayakawa, H., Fujimoto, M., Laakso, H., Novara, M., Ziethe, R., 2010. BepiColombo—Comprehensive exploration of Mercury: Mission overview and science goals. Planet. Space Sci. 58 (1-2), 2–20.

Britt, D.T., Pieters, C.M., 1994. Darkening in black and gas-rich ordinary chondrites: the spectral effects of opaque morphology and distribution. Geochim. Cosmochim. Acta 58 (18), 3905–3919.

Brunetto, R., 2009. Space weathering of small solar system bodies. Earth Moon Planet. 105, 249–255.

Brunetto, R., Lantz, C., Nakamura, T., Baklouti, D., Le Pivert-Jolivet, T., Kobayashi, S., Borondics, F., 2020. Characterizing irradiated surfaces using IR spectroscopy. Icarus 113722.

Charlier, B., Namur, O., 2019. The origin and differentiation of planet Mercury. Elements 15 (1), 9–14.

Christoffersen, R., McKay, D.S., Keller, L.P., 1996. Microstructure, chemistry, and origin of grain rims on ilmenite from the lunar soil finest fraction. Meteorit. Planet. Sci. 31 (6), 835–848.

Cintala, M.J., 1992. Impact-induced thermal effects in the lunar and Mercurian regoliths. J. Geophys. Res. Planets 97 (E1), 947–973.

Cintala, Mark J., DECEMBER 25, 1993. Impact-Induced Thermal Effects in the Lunar and Mercurian Regoliths. Journal of Geophysical Research 98 (El2), 23,603.

Domingue, D.L., Chapman, C.R., Killen, R.M., Zurbuchen, T.H., Gilbert, J.A., Sarantos, M., Orlando, T.M., 2014. Mercury's weather-beaten surface: understanding Mercury in the context of lunar and asteroidal space weathering studies. Space Science Reviews 181 (1-4), 121–214.

Ebert, M., Hecht, L., Deutsch, A., Kenkmann, T., 2013. Chemical modification of projectile residues and target material in a MEMIN cratering experiment. Meteorit. Planet. Sci. 48 (1), 134–149.

Farrell-Turner, S., Reimold, W.U., Nieuwoudt, M., Erasmus, R.M., 2005. Raman spectroscopy of olivine in dunite experimentally shocked to pressures between 5 and 59 GPa. Meteoritics & amp; Planetary Science 40 (9-10), 1311–1327.

Güldemeister, N., Wünnemann, K., Durr, N., Hiermaier, S., 2013. Propagation of impact - induced shock waves in porous sandstone using mesoscale modeling. Meteorit. Planet. Sci. 48 (1), 115–133.

Hamilton, V.E., 2010. Thermal infrared (vibrational) spectroscopy of Mg−Fe olivines: a review and applications to determining the composition of planetary surfaces. Geochemistry 70 (1), 7–33.

Hapke, B., 2001. Space weathering from Mercury to the asteroid belt. J. Geophys. Res. Planets 106 (E5), 10039–10073.

Hapke, B., Danielson, G.E., Klaasen, K., Wilson, L., 1975. Photometric observations of Mercury from Mariner 10. J. Geophys. Res. 80 (17), 2431–2443.

Harries, D., Yakame, S., Karouji, Y., Uesugi, M., Langenhorst, F., 2016. Secondary submicrometer impact cratering on the surface of asteroid 25143 Itokawa. Earth and Planetary Science Letters 450, 337–345.

Hiesinger, H., Helbert, J., Team, M.C.I., 2010. The Mercury radiometer and thermal infrared spectrometer (MERTIS) for the BepiColombo mission. Planet. Space Sci. 58 (1–2), 144–165.

Hiesinger, H., Helbert, J., Alemanno, G., Bauch, K., D'Amore, M., Maturilli, A., Morlok, A., Reitze, M.R., Stangarone, C., Stojic, A.N., Varatharajan, I., Weber, I., the MERTIS Co-I Team, 2020. Studying the composition and mineralogy of the hermean surface with the Mercury Radiometer and Thermal Infrared Spectrometer (MERTIS) for the BepiColombo Mission: an update. Space Sci. Rev. 216 (6), 1–37.

Hiesinger, H., Helbert, J., Team, M.C.I., 2010. The Mercury radiometer and thermal infrared spectrometer (MERTIS) for the BepiColombo mission. Planetary and Space Science 58 (1-2), 144–165.

Hirata, N., Kurita, K., Sekine, T., 2009. Simulation experiments for shocked primitive materials in the Solar System. Physics of the Earth and Planetary Interiors 174 (1-4), 227–241.

Hofmeister, A.M., 1987. Single-crystal absorption and reflection infrared spectroscopy of forsterite and fayalite. Phys. Chem. Miner. 14, 499–513. https://doi.org/10.1007/BF00308285.

Hofmeister, A.M., 1997. Infrared reflectance spectra of fayalite, and absorption data from assorted olivines, including pressure and isotope effects. Physics and Chemistry of Minerals 24 (7), 535–546.

Iishi, K., 1978. Lattice dynamics of forsterite. American Mineralogist 63 (11-12), 1198–1208.

Jarosewich, E., Nelen, J.A., Norberg, J.A., 1980. Reference samples for electron microprobe analysis. Geostand. Newslett. 4 (1), 43–47.

Jeanloz, R., Ahrens, T.J., Lally, J.S., Nord, G.L., Christie, J.M., Heuer, A.H., 1977. Shock - produced olivine glass: first observation. Science 197 (4302), 457–459.

Keller, L.P., McKay, D.S., 1993. Discovery of vapor deposits in the lunar regolith. Science 261 (5126), 1305–1307.

Kohout, T., Gritsevich, M., Grokhovsky, V.I., Yakovlev, G.A., Haloda, J., Halodova, P., Muinonen, K., 2014. Mineralogy, reflectance spectra, and physical properties of the Chelyabinsk LL5 chondrite−Insight into shock-induced changes in asteroid regoliths. Icarus 228, 78–85.

Kohout, T., Petrova, E.V., Yakovlev, G.A., Grokhovsky, V.I., Penttila, A., Maturilli, A.,¨ Zamyatin, D.A., 2020. Experimental constraints on the ordinary chondrite shock darkening caused by asteroid collisions. Astronomy & amp; Astrophysics 639, A146.

Kowitz, A., Schmitt, R.T., Uwe Reimold, W., Hornemann, U., 2013. The first MEMIN shock recovery experiments at low shock pressure (5–12.5 GPa) with dry, porous sandstone. Meteorit. Planet. Sci. 48 (1), 99–114.

Laetsch, T., Downs, R., 2006. Software for identification and refinement of cell parameters from powder diffraction data of minerals Using the RRUFF project and American mineralogist crystal structure databases. In: Abstracts from the 19th General Meeting of the International Mineralogical Association, Kobe, Japan, 23-28 July 2006.

Lane, M.D., Glotch, T.D., Dyar, M.D., Pieters, C.M., Klima, R., Hiroi, T., Sunshine, J., 2011. Midinfrared spectroscopy of synthetic olivines: thermal emission, specular and diffuse reflectance, and attenuated total reflectance studies of forsterite to fayalite. J. Geophys. Res. Planets 116 (E8).

Langenhorst, F., Deutsch, A., 1994. Shock experiments on pre-heated α-and β-quartz: I. Optical and density data. Earth and Planetary Science Letters 125 (1-4), 407–420.

Langenhorst, F., Deutsch, A., 2012. Shock metamorphism of minerals. Elements 8 (1), 31–36.

Lantz, C., Clark, B.E., Barucci, M.A., Lauretta, D.S., 2013. Evidence for the effects of space weathering spectral signatures on low albedo asteroids. Astron. Astrophys. 554, A138.

Lantz, C., Brunetto, R., Barucci, M.A., Fornasier, S., Baklouti, D., Bourçois, J., Godard, M., 2017. Ion irradiation of carbonaceous chondrites: a new view of space weathering on primitive asteroids. Icarus 285, 43–57.

Loeffler, M.J., Dukes, C.A., Baragiola, R.A., 2009. Irradiation of olivine by 4 keV He+: simulation of space weathering by the solar wind. J. Geophys. Res. Planets 114 (E3).

Loeffler, M.J., Dukes, C.A., Christoffersen, R., Baragiola, R.A., 2016. Space weathering of silicates simulated by successive laser irradiation: in situ reflectance measurements of Fo90, Fo99+, and SiO2. Meteorit. Planet. Sci. 51 (2), 261–275.

Lucey, P.G., Riner, M.A., 2011. The optical effects of small iron particles that darken but do not redden: evidence of intense space weathering on Mercury. Icarus 212 (2), 451–462.

Marchi, S., Brunetto, R., Magrin, S., Lazzarin, M., Gandolfi, D., 2005. Space weathering of near-Earth and main belt silicate-rich asteroids: observations and ion irradiation experiments. Astronomy & Astrophysics 443 (3), 769–775.

Martin, D.J., Pernet-Fisher, J.F., Joy, K.H., Wogelius, R.A., Morlok, A., Hiesinger, H., 2017. Investigating the shock histories of lunar meteorites Miller Range 090034, 090070, and 090075 using petrography, geochemistry and micro-FTIR spectroscopy. Meteorit. Planet. Sci. 52 (6), 1103–1124.

Matsumoto, T., Tsuchiyama, A., Uesugi, K., Nakano, T., Uesugi, M., Matsuno, J., Nakamura, T., 2016. Nanomorphology of Itokawa regolith particles: application to space-weathering processes affecting the Itokawa asteroid. Geochimica et cosmochimica acta 187, 195–217.

Moroz, L.V., Maturilli, A., Helbert, J., Sasaki, S., Bischoff, A., Jessberger, E.K., 2007. Mercury analogue materials: spectral reflectance, its comparison with TIR spectral emission, and a space weathering simulation experiment. Lunar Planet. Sci. Conf. 38, 1741.

Morlok, A., Bischoff, A., Patzek, M., Sohn, M., Hiesinger, H., 2017. Chelyabinsk −a rock with many different (stony) faces: An infrared study. Icarus 284, 431–442.

Morlok, A., Hamann, C., Martin, D.J.P., Joy, K.H., Wogelius, R., Weber, I., Helbert, J., 2019. MID-INFRARED INVESTIGATIONS OF LASER PRODUCED IMPACT MELT ANALOGS OF BASALT. LPI 2132, 2417.

Ness, N.F., Behannon, K.W., Lepping, R.P., Whang, Y.C., Schatten, K.H., 1974. Magnetic field observations near Venus: preliminary results from Mariner 10. Science 183 (4131), 1301–1306.

Nittler, L.R., Starr, R.D., Weider, S.Z., McCoy, T.J., Boynton, W.V., Ebel, D.S., Lawrence, D.J., 2011. The major-element composition of Mercury's surface from MESSENGER X-ray spectrometry. Science 333 (6051), 1847–1850.

Noble, S.K., Pieters, C.M., 2003. Space weathering on Mercury: implications for remote sensing. Sol. Syst. Res. 37 (1), 31–35.

Noble, S.K., Keller, L.P., Pieters, C.M., 2005. Evidence of space weathering in regolith breccias I: lunar regolith breccias. Meteorit. Planet. Sci. 40 (3), 397–408.

Noble, S.K., Keller, L.P., Christoffersen, R., Rahman, Z., 2015. The microstructure of a micrometeorite impact into lunar olivine. LPICo 1878, 2034.

Noel, Y., Catti, M., D'Arco, P., Dovesi, R., 2006. The vibrational frequencies of forsterite Mg 2 SiO 4: An all-electron ab initio study with the CRYSTAL code. Physics and Chemistry of Minerals 33 (6), 383–393.

Noguchi, T., Nakamura, T., Kimura, M., Zolensky, M.E., Tanaka, M., Hashimoto, T., Abe, M., 2011. Incipient space weathering observed on the surface of Itokawa dust particles. Science 333 (6046), 1121–1125.

Peplowski, P.N., Stockstill-Cahill, K., 2019. Analytical identification and characterization of the major geochemical Terranes of Mercury's northern hemisphere. J. Geophys. Res. Planets 124 (9), 2414–2429.

Pieters, C.M., Noble, S.K., 2016. Space weathering on airless bodies. J. Geophys. Res. Planets 121 (10), 1865–1884.

Pieters, C.M., Taylor, L.A., 2003. Systematic global mixing and melting in lunar soil evolution. Geophys. Res. Lett. 30 (20).

Pieters, C.M., Taylor, L.A., Noble, S.K., Keller, L.P., Hapke, B., Morris, R.V., Wentworth, S., 2000. Space weathering on airless bodies: Resolving a mystery with lunar samples. Meteoritics & Planetary Science 35 (5), 1101–1107.

Pillinger, C.T., 1979. Solar-wind exposure effects in the lunar soil. Rep. Prog. Phys. 42 (5), 897.

Reynard, B., 1991. Single-crystal infrared reflectivity of pure Mg 2 SiO₂ forsterite and (Mg 0.86, Fe 0.14) 2 SiO₄ olivine. Phys. Chem. Miner. 18 (1), 19–25.

Rubin, A.E., 1992. A shock-metamorphic model for silicate darkening and compositionally variable plagioclase in CK and ordinary chondrites. Geochim. Cosmochim. Acta 56 (4), 1705–1714.

Salisbury, J.W., D'Aria, D.M., Jarosewich, E., 1991. Midinfrared (2.5–13.5 μm) reflectance spectra of powdered stony meteorites. Icarus 92 (2), 280–297.

Sandt, C., Dionnet, Z., Toplak, M., Fernandez, E., Brunetto, R., Borondics, F., 2019. Performance comparison of aperture-less and confocal infrared microscopes. Journal of Spectral Imaging 8.

Sasaki, S., Hiroi, T., Nakamura, K., Hamabe, Y., Kurahashi, E., Yamada, M., 2002. Simulation of space weathering by nanosecond pulse laser heating: Dependence on mineral composition, weathering trend of asteroids and discovery of nanophase iron particles. Advances in Space Research 29 (5), 783–788.

Schmitt, R.T., 2000. Shock experiments with the H6 chondrite Kernouv´e: pressure calibration of microscopic shock effects. Meteorit. Planet. Sci. 35 (3), 545–560.

Servoin, J.L., Piriou, B., 1973. Infrared reflectivity and Raman scattering of Mg2SiO4 single crystal. physica status solidi (b) 55 (2), 677–686.

Siebert, H., 2013. Anwendungen der Schwingungsspektroskopie in der anorganischen Chemie. Springer-Verlag, 7.

Stoffler, D., Keil, K., RD, S.E., 1991. Shock metamorphism of ordinary chondrites.¨ Geochimica et Cosmochimica Acta 55 (12), 3845–3867.

Stoffler, D., Hamann, C., Metzler, K., 2018. Shock metamorphism of planetary silicate¨ rocks and sediments: proposal for an updated classification system. Meteorit. Planet. Sci. 53 (1), 5–49.

Stoffler, D., Hamann, C., Metzler, K., 2019. Addendum to¨ "Stoffler, D., Hamann, C.,¨ & Metzler, K. shock metamorphism of planetary silicate rocks and sediments: proposal for an updated classification system. Meteoritics & Planetary Science, 53(1), 5-49, 2018". Meteorit. Planet. Sci. 54 (4), 946–949.

Van der Bogert, C.H., Schultz, P.H., Spray, J.G., 2003. Impact-induced frictional melting in ordinary chondrites: a mechanism for deformation, darkening, and vein formation. Meteorit. Planet. Sci. 38 (10), 1521–1531.

Vance, A.M., Christoffersen, R., Keller, L.P., Berger, E.L., Noble, S.K., 2016. Evolution of Shock Melt Compositions in Lunar Regoliths. LPS XXXXVII, Conference paper.

Walker, R.J., Papike, J.J., 1982. The relationship of the lunar regolith less than 10-microns fraction and agglutinates. II-Chemical composition of agglutinate glass as a test of the "fusion of the finest fraction"/F3/model. Lunar Planet. Sci. Conf. Proc. 12, 421–432.

Weber, I., Morlok, A., Bischoff, A., Hiesinger, H., Ward, D., Joy, K.H., Crowther, S.A., Jastrzebski, N.D., Gilmour, J.D., Clay, P.L., Wogelius, R.A., Greenwood, R.C., Franchi, I.A., Münker, C., 2016. Cosmochemical and spectroscopic properties of Northwest Africa 7325—A consortium study. Meteoritics & Planetary Science 51 (1), 3–30.

Weber, I., Morlok, A., Heeger, M., Adolphs, T., Reitze, M.P., Hiesinger, H., Helbert, J., 2019. Excimer Laser Experiments on Mixed Silicates Simulating Space Weathering on Mercury. EPSC. EPSC-DPS2019.

Weider, S.Z., Nittler, L.R., Starr, R.D., McCoy, T.J., Stockstill-Cahill, K.R., Byrne, P.K., Solomon, S.C., 2012. Chemical heterogeneity on Mercury's surface revealed by the MESSENGER X-Ray Spectrometer. J. Geophys. Res. Planets 117 (E12).

Yamada, M., Sasaki, S., Nagahara, H., Fujiwara, A., Hasegawa, S., Yano, H., Otake, H., 1999. Simulation of space weathering of planet-forming materials: Nanosecond pulse laser irradiation and proton implantation on olivine and pyroxene samples.

Earth, Planets, and Space 51 (11), 1255–1265.

Zeng, X., Li, X., Martin, D., Tang, H., Yu, W., Liu, J., Wang, S., 2019. Micro-FTIR spectroscopy of lunar pyroclastic and impact glasses as a new diagnostic tool to discern them. J. Geophys. Res. Planets 124 (12), 3267–3282.